In–situ quantification of mechanical and permeability properties on outcrop analogues of offshore fractured and weathered crystalline basement: Examples from the Rolvsnes granodiorite, Bømlo, Norway

Published Version:
Ceccato, A., Viola, G., Tartaglia, G., Antonellini, M. (2021). In–situ quantification of mechanical and permeability properties on outcrop analogues of offshore fractured and weathered crystalline basement: Examples from the Rolvsnes granodiorite, Bømlo, Norway. MARINE AND PETROLEUM GEOLOGY, 124(104859), 1-20 [10.1016/j.marpetgeo.2020.104859].

Availability:
This version is available at: https://hdl.handle.net/11585/784466 since: 2020-12-15

Published:
DOI: http://doi.org/10.1016/j.marpetgeo.2020.104859

Ceccato, Alberto; Viola, Giulio; Tartaglia, Giulia; Antonellini, Marco: *In–situ quantification of mechanical and permeability properties on outcrop analogues of offshore fractured and weathered crystalline basement: Examples from the Rolvsnes granodiorite, Bømlo, Norway*

MARINE AND PETROLEUM GEOLOGY VOL.124 ISSN 0264-8172

DOI: 10.1016/j.marpetgeo.2020.104859

In–situ quantification of mechanical and permeability properties on outcrop analogues of offshore fractured and weathered crystalline basement: Examples from the Rolvsnes granodiorite, Bømlo, Norway

Alberto Ceccato*, Giulio Viola*, Giulia Tartaglia, Marco Antonellini

* Corresponding Authors; email: alberto.ceccato@unibo.it; giulio.viola3@unibo.it

Dipartimento di Scienze Biologiche, Geologiche ed Ambientali – BiGeA, Alma Mater Studiorum – Università di Bologna – via Zamboni, 67, 40126 Bologna, Italy

Abstract

Fractured and weathered crystalline basement units below erosional unconformities potentially represent unconventional reservoirs for georesources (oil, mineral and water). The reservoir properties and characteristics strongly depend on secondary processes connected to the local structural and alteration/weathering history. Here we present the results of in–situ field quantification of mechanical (uniaxial compressive strength) and petrophysical (permeability) properties of a fractured and weathered crystalline basement at selected outcrops on the island of Bømlo (western Norway). The Bømlo outcrops are believed to represent an onshore analogue of the unconventional oil reservoir hosted in the offshore Utsira High granodioritic fractured basement (northern North Sea). The off– and onshore crystalline basements have both undergone surficial weathering during the Mesozoic, as shown by the occurrence of a dated, variably thick saprolitic profile on top of fresh fractured basement blocks. The Bømlo crystalline basement is characterized by a complex and highly permeable fracture network. Fault rocks within its fault zones are characterised by an anisotropic mechanical strength and by an average permeability that is two orders of magnitude larger than that of the host rock. The matrix permeability and mechanical strength are significantly affected by alteration/weathering products. Analysis of the textural and mineralogical characteristics of the weathered outcrops allowed us to constrain the variation of permeability and mechanical strength as a function of increasing alteration and to infer their distribution in the, now eroded, top–basement weathering profile on Bømlo. Weathering enhances permeability and drastically decreases the mechanical strength. Nevertheless, evolved saprolitic horizons may act as low–permeability top–seal units to the fractured and weathered crystalline basement reservoir. The obtained permeability and mechanical data are finally used to better constrain the potential reservoir rocks, the fluid migration pathways, and to discuss their role in the geomechanics of a conceptualised fractured and weathered crystalline basement unconventional reservoir.

Keywords

Fractured basement reservoir; Saprolite; Utsira High; Fault rock permeability.

1. Introduction

Faults, fractures, and related alteration zones control fluid transport within low–permeability crystalline basement rocks at different crustal levels within all tectonic settings and geological conditions (Stober and Bucher, 2015). Indeed, brittle deformation and alteration processes may drastically affect the mechanical strength and permeability of inherently stiff, low–permeability crystalline basement rocks through the development of secondary porosity (Brace, 1984; Bruhn et al., 1994; Caine et al., 1996; Stober and Bucher, 2007; Place et al., 2016; Staněk and Géraud, 2019). A better understanding of how these processes affect the rock mechanical strength and the properties controlling fluid flow is, therefore, of interest to geoscientific research and many applied fields. Examples are the geological characterisation necessary to the construction of deep nuclear waste and CO_2 repositories (Armitage et al., 2013), the better definition of crustal rheology and rock mechanics (Caine et al., 1996; Sibson and Rowland, 2003) and the exploration and production of georesources (Dewandel et al., 2006; Stober and Bucher, 2015; Kitchka et al., 2017). Specific to this last point, in the recent past, economically viable unconventional oil plays have been defined in structural highs within fractured and weathered crystalline basement blocks (Koning, 2003; Luthi, 2005; Kitchka et al., 2017; Braathen et al., 2018; Bonter and Trice, 2019; Holdsworth et al., 2019, 2020; Trice et al., 2019; McCaffrey et al., 2020). There, the constituent elements of a reservoir include (Riber et al., 2015, 2017; Fredin et al., 2017b; Braathen et al., 2018; Lothe et al., 2018; Walter et al., 2018; McCaffrey et al., 2020): (1) the host crystalline rock, characterised by primary low–porosity/permeability; (2) fractures, fault zones, mineral veins and open fissures characterised by enhanced micro– and mesoscopic fracture porosity; (3) fluid–rock interaction zones related to either alteration along structural discontinuities or to top–basement paleo–weathering profiles; (4) the buffering/sealing fault zones bounding the structural highs; (5) the sedimentary cover overlying the weathered crystalline basement acting as either reservoir rock, top–seal and/or source rock. The reservoir rock consists of the fractured and altered/weathered crystalline basement, in which fluid storage and transport are dependent mainly on the spatial arrangement, geometry and distribution of "matrix" and "structural" permeability (Braathen et al., 2018; Trice et al., 2019). The "matrix" permeability is directly related to the textural, compositional, and alteration characteristics of the host crystalline basement (Bruhn et al., 1994; Géraud et al., 2010; Braathen et al., 2018). The "structural" permeability, on the other hand, reflects and is related to the presence of structural discontinuities at all scales, from microfractures to crustal–scale fracture and fault zones (Bruhn et al., 1994; Sibson and Rowland, 2003; Holdsworth et al., 2020). Brittle faulting and fluid percolation within structural discontinuities may either increase and/or decrease the matrix permeability of the host crystalline basement (Bruhn et al., 1994; Caine et al., 1996; Holdsworth et al., 2019, 2020; McCaffrey et al., 2020). The geological conditions (depth, pressure, temperature) and the origin (metamorphic, hydrothermal, or meteoric) of fluids may lead to different brittle fault rock development and different types of alteration from textural and compositional points of view (Steefel and Mäher, 2009).

The nature, spatial arrangement, and geometry of structural and textural features at the reservoir scale are commonly defined through seismic geophysical investigations. Textural variations, fracture, and fault zones displaying sufficient seismic impedance contrast as well as fault thickness or throws > 4–10 m are usually detected by reservoir–scale seismic investigations and are thus classified as seismic–resolution–scale (SRS) features (Tanner et al., 2019). However, the site– (well–, borehole– or tunnel–) scale fluid transport and storage capabilities are effectively controlled by sub–seismic–resolution scale (SSRS) features (thickness/throw <4–10 m; Damsleth et al., 1998; Walsh et al., 1998).

In–situ analysis of outcrop analogues of onshore fractured and weathered basement blocks may provide the unique opportunity to characterise the details of the petrophysical and mechanical properties of SSRS features and to understand their relationships with larger, reservoir–scale SRS features (Jones et al., 2008; Howell et al., 2014; McCaffrey et al., 2020; Primaleon et al., 2020). We present here the results of the in–situ structural, geomechanical (uniaxial compressive strength, UCS), and petrophysical (permeability, k) characterisation of selected outcrops of fractured and weathered crystalline basement rocks on the island of Bømlo, western Norway (Fig. 1a–b). The crystalline basement on Bømlo is being currently studied as the potential onshore analogue of fractured and weathered basement reservoirs of the Utsira High, an economically viable unconventional reservoir located offshore western Norway in the northern North Sea (Figs. 1a–2a; Banks et al., 2019; Trice et al., 2019). The crystalline basement on Bømlo consists of igneous (granodiorite, granite and gabbro) and volcano–sedimentary units of Ordovician–Silurian age belonging to the Upper Allochthon of the Caledonian orogen (Slagstad et al., 2011). From the Permian onward, the crystalline basement on Bømlo underwent a series of brittle deformation events (Scheiber and Viola, 2018) and experienced pervasive alteration/weathering in response to subaerial exposure in tropical humid climate conditions during the Triassic, forming a thick weathering profile (Fredin et al., 2017b). Similarly, the offshore Utsira High reservoir is characterised by a pervasively fractured crystalline basement, mainly composed of felsic intrusive and gabbroic rocks of Ordovician–Silurian age (Slagstad et al., 2011; Riber et al., 2015), on top of which rests a paleo–weathering profile formed during the late Triassic (Fredin et al., 2017b; Riber et al., 2017; Lothe et al., 2018) (Fig. 2b).

On Bømlo, we have worked on a few selected outcrops (Fig. 1c) that are representative of (1) structural discontinuities affecting the crystalline basement "matrix" properties at different scales, from SSRS fracture corridors to SRS fault zones (Fig. 2c) and (2) textural heterogeneities related to the progressive development of alteration/weathering products(Fig. 2b). Our analyses aimed specifically at the characterisation of the different structural and alteration products controlling the current "matrix" mechanical and permeability properties of the crystalline basement at the sub–seismic–resolution scale. The role of the different structural and alteration elements in controlling fluid transport and storage, and the characterisation of potential reservoir rocks in fractured and weathered crystalline basement structural highs, are then discussed to the benefit of broader, more general conceptual scenarios.

Quantitative, high–resolution geomechanical and petrophysical datasets are quite rare, yet fundamental for interpreting increasingly higher–resolution geophysical datasets, for reducing the uncertainty in reservoir modelling, for better constraining fault zone mechanics and for assessing borehole stability during exploration and drilling (Rutqvist and Stephansson, 2003; Wibberley et al., 2008; Steer et al., 2011; Jeanne et al., 2017). Our results are thus useful to help bridge the gap between field observations and large–scale geological contexts, where the lack of direct access to the geological objects of interest and the processes determining their spatial and temporal evolution commonly preclude straightforward across–scale correlations and quantifications. In addition, the geological/structural contextualisation offered by the quantitative, high–resolution dataset presented here may help to better read and interpret the at times overwhelming wealth of global and regional geomechanical/petrophysical datasets (Lothe et al., 2018; Walter et al., 2018; Scibek, 2020).

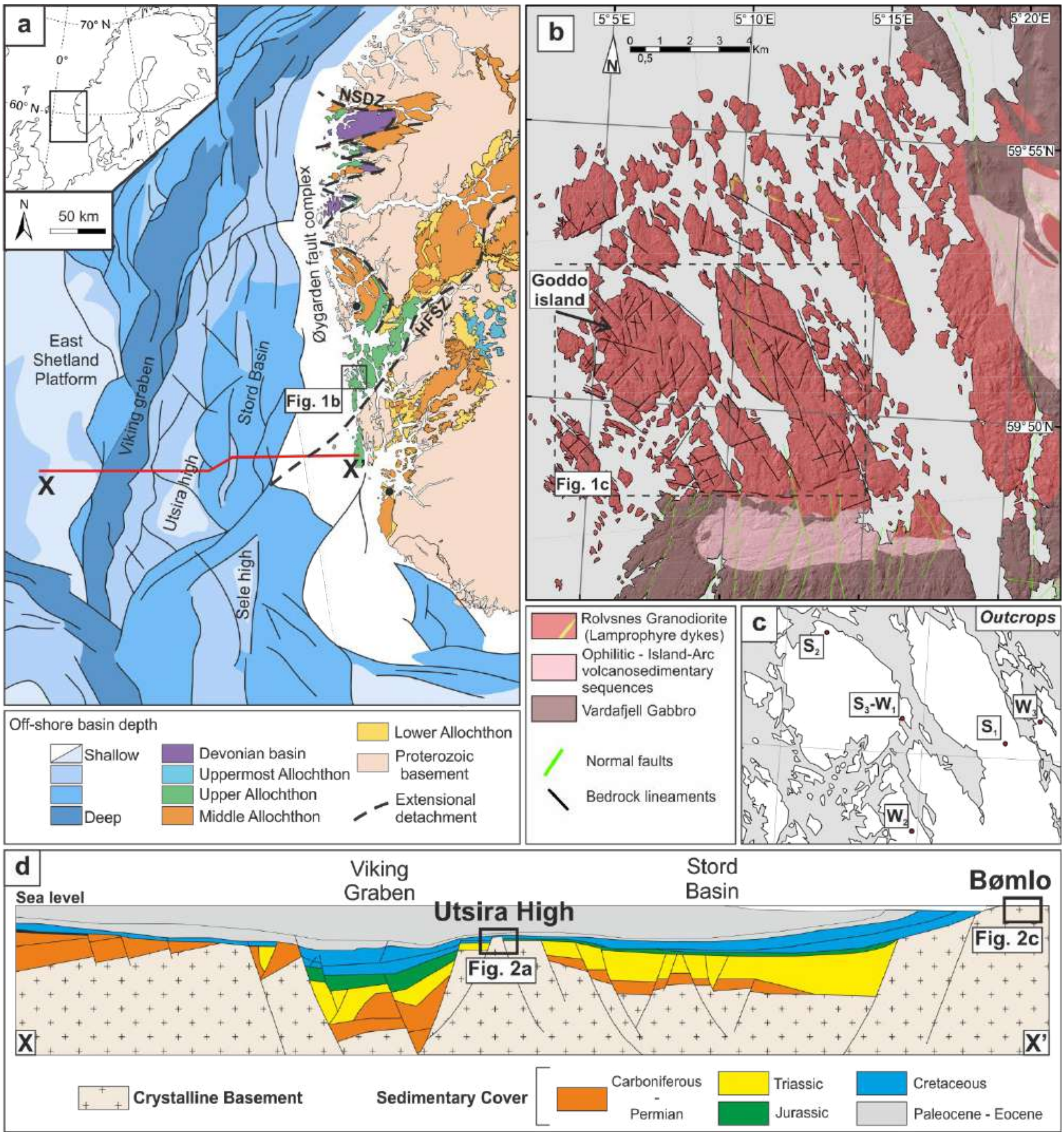

Figure 1: (a) Geological map of southwestern Norway and the northern North Sea (modified after Slagstad et al., 2011; Scheiber and Viola, 2018). HFSZ: Hardangerfjord Shear Zone; NSDZ: Nordfjord–Sogn Detachment Zone. The red line X–X' represents the trace of the geological cross section presented in Fig. 1d. (b) Geological map of the northern Bømlo area, including the island of Goddo (redrawn from the NGU geological map of Norway 1:50000). (c) Simplified topographic map of Bømlo showing the locations of the studied outcrops. (d) Schematic geological cross section through the central North Sea (X–X' in (a)) (modified from Riber et al., 2015).

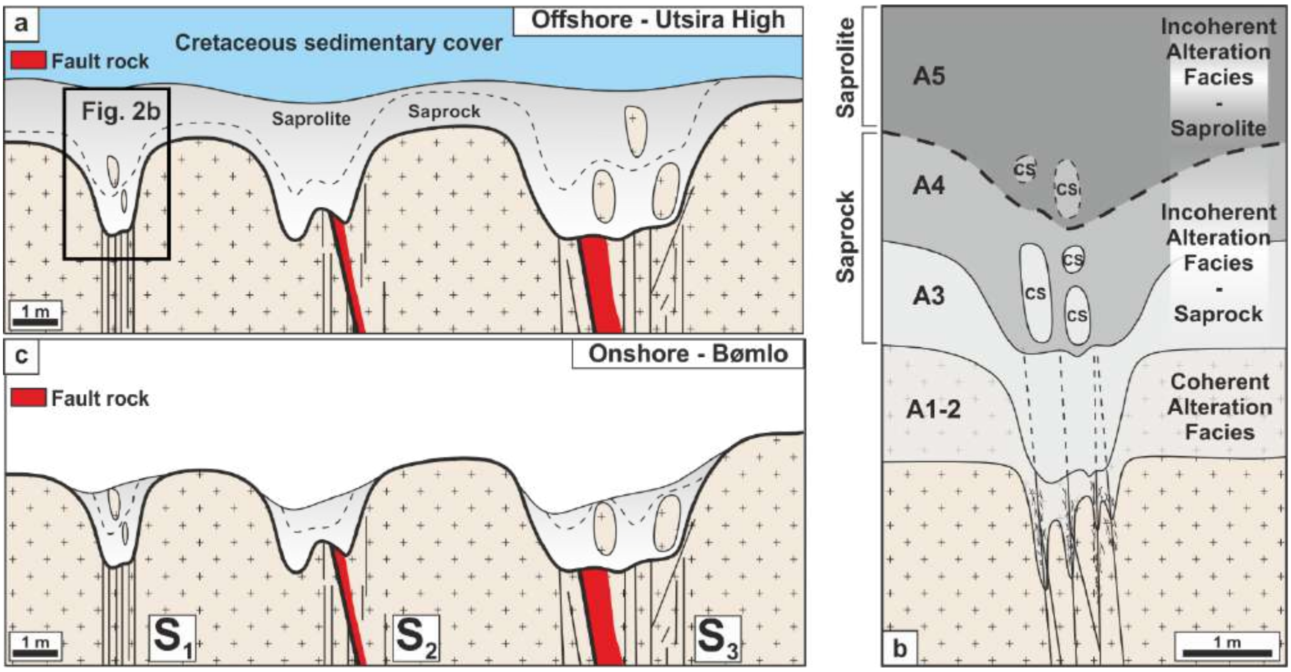

Figure 2: (a) Simplified schematic representation of the fractured and weathered basement top section preserved offshore in the Utsira High beneath the Mesozoic sedimentary cover. This schematic representation focuses on the fractured crystalline basement, which is characterised by different typologies of fractures and fault zones, the weathering profile (saprock–saprolite in grey) and the overlying sedimentary cover (light blue). The dashed line represents the boundary between saprock and saprolite within the weathering profile. (b) Simplified sketch of the top–basement weathering profile showing the gradual transition from unaltered and fractured host rock at the base of the profile, toward saprock and saprolite at the top. The weathering profile locally reaches greater depths where in correspondence with structural discontinuities (in this case, a SSRS fracture corridor, S_1 of Fig. 2a and 2c). The progression of weathering is illustrated by the continuous darkening of the grey shades and the increasing number in the alteration/weathering grade on the left (A1–A5). (CS: core stones). (c) Simplified schematic representation of the fractured and weathered basement top section now exposed onshore on the island of Goddo. The erosion of the weathering profile has led to the exposure of an "etched" basement top surface (Fredin et al., 2017). S_1, S_2 and S_3 represent the three typologies

of deformation structures studied in this work. S_1: SSRS fracture corridors; S_2: SSRS fault zone; S_3: SRS fault zone.

2. Geological setting

The crystalline basement rocks exposed on the island of Bømlo in western Norway belong to the Upper Allochthon units of the Caledonian orogen (Gee et al., 2008) (Fig. 1a). They mainly consist of variably metamorphosed igneous, volcanic and sedimentary units derived from the Iapetus oceanic domain (Roberts, 2003). The study area is located within the Rolvsnes granodiorite (RGD, 466 ± 3 Ma, U/Pb on zircon) (Scheiber et al., 2016), a plutonic body related to pre–Scandian magmatism that intrudes the ophiolitic, gabbroic, and volcano–sedimentary orogenic units (Slagstad et al., 2011) (Fig. 1b). After its emplacement in the Ordovician, the RGD remained at shallow crustal levels (< 10–15 km depth), thus escaping pervasive ductile deformation and metamorphic re–equilibration during the Scandian tectonometamorphic event (Scheiber et al., 2016; Scheiber and Viola, 2018). During the post–Caledonian orogenic collapse and extension, the Upper Allochthon units in the Bømlo region belonged to the hanging wall of the Hardangerfjord Shear Zone, a regional NW–dipping extensional detachment reactivating earlier Caledonian thrusts and nappe contacts (Fig. 1a) (Fossen and Hurich, 2005). The RGD recorded a prolonged and multi–phased brittle deformation history, which has been characterised in detail by means of structural and geochronological analysis of the different fracture patterns exposed on Bømlo (Scheiber et al., 2016; Scheiber and Viola, 2018).

2.1 Brittle deformation and alteration history of the Bømlo basement

The latest stages of Caledonian compression during the Mid Ordovician–Silurian are recorded by ENE–WSW–striking reverse and kinematically consistent conjugate sets of strike–slip shear fractures and minor faults accompanied by the emplacement of greisens, dykes, and mineralised veins (Scheiber et al., 2016). A first phase of NW–SE extension occurred during the Devonian in response to Caledonian orogenic collapse, as recorded by the development of minor, NE–SW–striking normal faults. Ordovician to Devonian mineralised veins, joints, shear fractures, and minor faults are pervasive and widely distributed, and they are commonly filled with– and sealed by a variety of minerals. In the Permian–Early Cretaceous, the area underwent renewed regional extension related to the long–lived series of E–W–directed North Sea rifting events. The first main North Sea rifting stage is recorded by the development of widespread NE–dipping normal faults active during Permian to Triassic times (Viola et al., 2016; Scheiber and Viola, 2018). This rifting event led to the formation of the most prominent structural highs and basins of the North Sea, namely the Stord Basin, Utsira High, and the Viking Graben (Bell et al., 2014; Scheiber and Viola, 2018). Rifting and crustal stretching continued during the Late Triassic and Jurassic leading to the formation of ENE–dipping normal faults associated with the deepening and development of the offshore Viking Graben (Scheiber and Viola, 2018) and the progressive reactivation of the previously formed NE–dipping normal faults (Viola et al., 2016). This rifting phase enhanced the rapid exhumation of the Bømlo crystalline basement from 6–8 km to shallow (<2 km) depths during Permian–to–Jurassic times (Scheiber and Viola, 2018). From the Late Jurassic onward, the crystalline basement has resided at very shallow depth (<2 km; Fredin et al., 2017b; Scheiber and Viola, 2018). Far–field stresses related to the Early Cretaceous rifting stage of the northern North Sea and the Mid–Norwegian margin subsequently led to the development of N–S–trending fracture corridors in the Bømlo region (Viola et al., 2016; Scheiber and Viola, 2018).

A distinctive characteristic of the Bømlo fractured crystalline basement is the occurrence of alteration and weathering products spatially related to fracture and fault zones (Viola et al., 2016; Fredin et al., 2017b; Scheiber and Viola, 2018). Altered/weathered granodiorite is invariably found as lenses along fractures and variably altered volumes within high–fracture density deformation zones. The dense network of fractures and fault zones likely promoted fluid infiltration at depth (Place et al., 2016). K–Ar dating of alteration–related authigenic illite has revealed the occurrence of multiple shallow–crustal levels alteration/weathering events during the prolonged and multi–phased brittle deformation history discussed above (Viola et al., 2016; Fredin et al., 2017b; Scheiber and Viola, 2018). A significant event occurred during the Late Triassic (ca. 220–200 Ma), when the fractured crystalline basement on Bømlo was exposed to sub–aerial alteration and formation of deep–weathering horizons (saprock – saprolite) related to the Mesozoic tropical–humid climate of the region (Fredin et al., 2017b). Other alteration events likely occurred in the Permian and Jurassic–Cretaceous (A. Margreth personal communication; Viola et al., 2016; Scheiber and Viola, 2018). The detailed genetic processes and geological conditions under which these latter alteration events occurred are still not well constrained (A. Margreth personal communication). Despite the possible diachronism and superposition of different alteration/weathering events, all the observed alteration products of the crystalline basement on Bømlo present similar field textural and mineralogical characteristics. Progressive disaggregation of the host RGD into sandy "grus–type" aggregates (*sensu* Migoń and Thomas, 2002) is commonly accompanied by mineral (feldspar) alteration and clay–mineral authigenesis. Such characteristics are ascribable to a process of arenitisation, kaolinitisation, and/or saprolitisation of the host RGD occurring at shallow crustal depths (< 6 km) up to surficial conditions (Viola et al., 2016; Fredin et al., 2017b, 2017a; Scheiber and Viola, 2018). It is indeed quite well known that hydrothermal kaolinitisation and saprolite formation under tropical–humid climate conditions may lead to alteration products with similar textural/mineralogical/mechanical characteristics (Coggan et al., 2013).

2.2 Onshore–offshore correlation – Bømlo basement and Utsira High

Alteration characteristics similar to those documented onshore have been detected in offshore exploratory wells from the Utsira High fractured crystalline basement at variable depth beneath the sedimentary cover (Riber et al., 2015; Trice et al., 2019). Amidst the central North Sea, the Utsira High represents a N–S trending basement structural high bounded by the Viking Graben to the west and the Stord Basin to the east (Fig. 1a, d) (Gabrielsen et al., 2001). The basement unit in its core is mainly composed of Ordovician–Silurian granitoid and gabbroid rocks (Riber et al., 2015). Petrological, geochronological, and geophysical data suggest that, prior to the opening of the North Sea, the crystalline basement of Bømlo and the basement units of the Utsira High likely belonged to the same unit of the Upper Allochthon (Slagstad et al., 2011; Lundmark et al., 2014; Riber et al., 2015; Fredin et al., 2017b; Lothe et al., 2018; Trice et al., 2019). The seismically imaged top–basement topography of the Utsira High shows the occurrence of widespread fracture lineaments and fault zones , resembling the onshore joint–aligned valley morphology of the Bømlo region (Fredin et al., 2017b). The pervasive and variably oriented fracture lineaments and fault zones thus suggest that, similarly to the onshore margin, the Utsira High also underwent a prolonged and multi–phased brittle deformation history (Fredin et al., 2017b). Brittle deformation probably started in the Permian–Triassic during the first rifting phase of the North Sea, and ended in the Cretaceous–Paleogene with the northward migration of the rifting activity toward the Mid–Norwegian margin (Bell et al., 2014; Scheiber and Viola, 2018). Offshore exploration wells have identified the occurrence of a variably preserved 1–10 m thick weathering profile atop of the fractured granitoid basement (Fig. 2a) (Riber et al., 2015; Trice et al., 2019). The weathering profile, from top to bottom, consists of (Fig. 2b) (Riber et al., 2015, 2016, 2017, 2019a): (i) clay–rich, saprolite – incoherent alteration facies A5 of Riber et al., (2016); (ii) grus–type saprock, in which the granitoid magmatic texture is still preserved – incoherent alteration facies A3–A4 of Riber et al., (2016); (iii) coherent, partially weathered granitoid, still preserving the magmatic texture and mechanical properties of the host rock – alteration facies A1–A2 of Riber et al., (2016). K–Ar dating on authigenic illite from core samples of the saprolitic level in the weathering profile has shown that the Utsira High crystalline basement was exposed to sub–aerial conditions and weathering during the Triassic (206 ± 4 Ma) (Fredin et al., 2017b).

After the Late Triassic, burial and sedimentation affected the whole passive margin (including the Utsira High and Bømlo region), causing the deposition of a several km thick Mesozoic sedimentary succession (Sclater and Christie, 1980; Gabrielsen et al., 2001; Bell et al., 2014). The buried Utsira High fractured–and–weathered basement acted as a system reservoir–trap for oil and currently, thus, represents an economically viable unconventional oil play (Trice et al., 2019). Offshore exploration wells have identified exploitable oil resources hosted in the basement–top weathering profile beneath the sedimentary cover (Fig. 2a–b) (Riber et al., 2015, 2017). Pre–Cretaceous SRS faults bound laterally the reservoir basement blocks, which are overlain by the Jurassic–Cretaceous sedimentary cover that acted as both lateral source rock and top–seal unit for oil–migration within the structural high (Trice et al., 2019). Jurassic–Cretaceous sedimentation likely affected also the Bømlo region, as inferred from the occurrence of Late–Mesozoic sedimentary basins close to the present–day onshore area (Fredin et al., 2017b, 2017a). Onshore, the Mesozoic sedimentary cover and the underlying Triassic top–basement weathering profile have been almost completely eroded by geomorphic and glaciogenic processes during the Cenozoic (Fredin et al., 2017b; Riber et al., 2017). As a consequence, only the deepest portions of the top–basement weathering profile are locally preserved, particularly where the effects of weathering penetrated for a few tens of m into the crystalline basement along discrete structural discontinuities (i.e. fracture and fault zones; Fig. 2c) (Fredin et al., 2017b). The deepest portion of the weathering profile, preserved in these structurally–controlled depressions may, therefore, have escaped from significant textural, mechanical, and mineralogical modifications related to the subsequent Cenozoic erosion, weathering or alteration (Fredin et al., 2017b, 2017a; Lothe et al., 2018)

For these reasons, an increasing number of multidisciplinary studies in the region considers the fractured and weathered crystalline basement exposed on Bømlo as a reliable onshore analogue of the offshore crystalline basement of the Utsira High (Fredin et al., 2017b; Lothe et al., 2018; Banks et al., 2019; Trice et al., 2019).

3. Methods

Our structural analysis focussed on the identification and characterisation of meso–scale fracture patterns and the definition of the main structural domains related to faulting. The investigation of petrophysical (permeability) and geomechanical (uniaxial compressive strength) properties has been carried out directly in the field on selected representative outcrops. In–situ permeability measurements have been carried out with a New England Research TinyPerm–3 air–minipermeameter on both fault rocks and alteration products related to basement weathering and saprolitisation. The minipermeameter is calibrated by the manufacturer with known standards. The instrument allows a reliable field investigation of rock permeability within small volumes (1–1.5 cm^3) in the 10^{-3}–10 D range, even though controlled laboratory tests have demonstrated its capability to measure permeability values as low as 10^{-5} D (Filomena et al., 2014). In the bulk–rock permeability mode, the instrument directly yields an estimate of the permeability based on the outgoing air flow rate from the built–in compression vessel. Permeability values obtained from air–minipermeametry need to be corrected and standardised in order to be comparable with permeability values obtained from laboratory tests on rock plugs or image analysis (Fossen et al., 2011; Filomena et al., 2014; Torabi et al., 2018). Air–minipermeameters yield either larger permeability values (by a factor of 1.7–1.8) when compared with results derived from image analysis quantifications (Fossen et al., 2011), or lower permeabilities (-37%) than those obtained from small (<10 cm) rock plugs used in laboratory tests (Filomena et al., 2014). In addition, permeability estimates from permeametry tests adopting a gas as permeating fluid (as in air–minipermeametry) can be significantly larger than the estimates from permeability tests relying on a liquid as permeating fluid as a consequence of possible slip–flow effects (Klinkenberg effect) (van Noort and Yarushina, 2019). This has to be considered when using absolute gas permeability values to analyse the flow of a liquid in the same porous medium.

The geomechanical characterisation has been carried out with a L–type Schmidt hammer (DRC GeoHammer, 0.735 N·m impact energy) calibrated according to international standards (ASTM D5873–00; EN 12 504–2; ASTM C 805–02). The reliability range of the instrument extends between 10 MPa and 300 MPa of UCS (Aydin and Basu, 2005).

We ran petrophysical and geomechanical analyses both on compositionally and texturally homogeneous volumes of the outcrops, thought to be representative of the bulk rock properties, and along transects. Where rock textural anisotropies were present, we performed permeability and Schmidt hammer analysis both perpendicular and parallel to the dominant planar rock fabric, aiming at evaluating the potential anisotropy of petrophysical and geomechanical properties. Transects allowed us to constrain the variation of the analysed properties across weathering fronts and high–density fracture zones. Surface spot analyses for both permeability and Schmidt hammer rebound analyses have been done by probing representative outcrop surfaces with at least 10 measurements. Selected measuring spots were at least 10–15 cm away from mesoscopic fractures wherever possible (Aydin and Basu, 2005). Both permeability and Schmidt hammer rebound analyses were repeated twice in the immediate surroundings of the selected spot along transects, for a total of three measurements. The replicates were not exactly on the same point to avoid results biased by subtle rock modifications (e.g., compaction and microfracturing) due to the previous measurements. Each measure spot was kept at c. 5–10 cm from the nearest measuring point both along transects and within selected areas, and taken to be representative of a 5 cm–radius hemispherical volume below it (ASRM standards; Aydin and Basu, 2005; Aydin, 2009; Demirdag et al., 2009). UCS values were retrieved from the analysis of Schmidt hammer rebound values (Aydin and Basu, 2005). Schmidt hammer measurements were carried out perpendicularly to clear, fresh rock surfaces (wherever possible), parallel to the horizontal direction. Schmidt hammer rebound values obtained from the in–situ measurement were converted into UCS by following the hammer orientation–dependent calibration curves provided by the manufacturer. Horizontal rebound values were converted into UCS by the following equation:

$$UCS = 0.0232*R^{2.2637} \text{ (MPa)}$$

Presented data are not corrected or standardised, so as to fully capture the heterogeneity and potential spread of rock mechanical properties (Aydin, 2009).

At one outcrop, fracture pattern characteristics have been quantified by using circular scan windows along a transect previously adopted for petrophysical and geomechanical analysis (Watkins et al., 2015). The results of fracture intensity (P_{21}) quantification from circular scan windows 10–cm–diameter have been compared with the along–transect variation of mechanical strength (Vignaroli et al., 2019). The same outcrop has been analysed also with a 1.4 m radius circular scan window to capture the outcrop scale characteristics of the fracture pattern. A schematic representation of the tectonic fractures of the outcrop has been obtained by line drawing on an outcrop field photo. The resulting line drawing has been analysed with FracPaQ (Healy et al., 2017) in order to quantify fracture intensity and 2D permeability at the outcrop scale in the direction of fluid flow (Long et al., 1982; Watkins et al., 2018).

4. Results

4.1 Outcrop description

On Bømlo, we have investigated five outcrops representative of the different deformation and weathering product end members, to constrain their mesoscopic structural characteristics as well as their petrophysical and geomechanical properties. Some of the analysed outcrops contain both structural and weathering features. For the clarity of presentation and discussion, outcrops are grouped into Group S (representative of *structural features*, S_1 to S_3) and Group W (*weathering features*, W_1 to W_3) (Figs. 1c, 2c–d). Magmatic dykes, greisens and mineralised veins are common in the RGD. The detailed characterisation of their mechanical strength and permeability properties is, however, beyond the scope of this paper.

Group S includes outcrops where we measured the geomechanical and petrophysical characteristics of discrete mesoscopic deformation zones (Fig. 2c). Our field investigations focussed mainly on the analysis of fracture corridors and major (either SSRS or SRS) fault zones formed during the Permian to Cretaceous interval, which significantly contributed to the development and modification of the crystalline basement permeability (Scheiber and Viola, 2018; McCaffrey et al., 2020). The pervasive and widely distributed Ordovician to Devonian mineralised joints, shear fractures and minor faults are commonly filled and sealed by different minerals (Scheiber and Viola, 2018), such that their contribution to the overall current permeability of the crystalline basement is assumed to be very limited (Watkins et al., 2018; McCaffrey et al., 2020). The field criteria adopted for the classification of different structures include: (i) the width of the deformation zone, as indicated by the across–strike thickness of the fractured domain; (ii) the occurrence/lack of fault rocks within the deformation zone; (iii) the width of the fault rock–bearing deformation zone (fault core). The width of the fault core may help us to quantify the minimum fault throw, and thus discriminate between SSRS and SRS deformation zones. The structural features included in Group S are: SSRS fracture corridors (S_1), a SSRS fault zone (S_2), and a SRS fault zone (S_3). Group S is numbered according to the increasing size of the studied structural features (fracture/fault zone width) as constrained by outcrop observations. The analysis of these outcrops allowed us to constrain the mechanical strength and permeability variation related to: (1) high–intensity fracture zones within (SSRS) fracture corridors; (2) fault rock development and distribution within SSRS and SRS fault cores.

Group W includes outcrops used to characterise the weathering features affecting the crystalline basement. Each Group W outcrop has already been previously analysed and sampled for illite K–Ar dating aiming at constraining the age of weathering (Viola et al., 2016; Fredin et al., 2017b; Scheiber and Viola, 2018). Results from XRD analysis (Table 1) reported in the cited references are here adopted to qualitatively characterise the mineral composition of weathering products. Group W includes: outcrop W_1 formed by partially altered RGD with incipient weathering and discolouring mainly localised along fractures; outcrop W_2 formed by cohesionless, altered RGD, still preserving the RGD magmatic structure but completely transformed into a sandy aggregate (saprock – grus); outcrop W_3 formed by cohesionless, altered RGD with increasing clay content (saprolite). The W outcrops are presented herein from W_1 to W_3 according to the increasing degree of weathering (from incipient to evolved weathering). The degree of weathering has been qualitatively deduced directly on the field comparing the mechanical/textural characteristics of the weathering products with those described by Riber et al. (2016) for the alteration facies of the Utsira High core samples. In all the analysed outcrops, alteration/weathering products invariably postdate the formation of brittle deformation zones.

4.1.1 Group S – Fractures and fault zones within the crystalline basement

Outcrop S_1. This outcrop contains a deformation zone defined by a 10–15 m thick fracture corridor. The central portion of the fracture corridor is characterised by a 2–5 m thick zone of high fracture–intensity (average fracture spacing = 0.05–0.1 m), composed of NNE–SSW–trending subvertical open fractures (Fig. 3a). Mesoscopic fractures are usually longer than 0.5–1 m along the dip direction, generally subparallel, but still locally forming a well–interconnected fracture network. Their typical aperture (*sensu* Ortega et al., 2006) is in the order of <1 mm. This deformation zone likely accommodated minor (<1m) lateral displacement, as inferred by the only local and rare development of fault striae (mainly strike–slip) on fracture surfaces and the limited offset (c. 6 cm) of crosscut magmatic markers (Scheiber and Viola, 2018). The outcrop is generally fresh, although fractures are in some cases filled with granular material probably related to either alteration or presence of fault rocks along the major fracture planes. The presence of now–eroded saprolite horizons has been inferred above the outcrop (Fig. 6g–h in Scheiber and Viola, 2018). The finest grain–size fractions of the alteration rock observed within the fractures are enriched in smectite–like clays of Jurassic age (187.5 ± 16.7 Ma; Table 1), as inferred from K–Ar dating on authigenic illite (sample TSC–1 of Scheiber and Viola, 2018). Alteration of the rock postdates the formation of the fracture corridor, which is thus older than Jurassic in age. The only limited throw (< 1 m) and width of the fracture corridor core (< 10 m) suggest that outcrop S_1 represents a SSRS fracture corridor.

Outcrop S_2. Outcrop S_2 contains two subparallel, well–localised SSRS fault zones characterised by a 10 cm thick cataclastic fault core (Fig. 6i–j in Scheiber and Viola, 2018). Each fault zone is characterised by a polished principal slip surface (PSS) oriented 70°/140° (dip/dip direction) (Fig. 3b). The PSS is decorated by transtensive–kinematics slickenlines plunging 30°/070° (plunge/trend). Several scattered, sub–vertical open fractures surround the fault core, defining a poorly developed 1–m–thick damage zone. Speculatively, the thickness of the fault core (10 cm) would be consistent with a fault throw in the order of 1–10 m (Torabi and Berg, 2011). The limited fault core width and estimated throw suggest that these fault zones may represent SSRS fault zones. The host RGD and the cataclastic core are locally altered, as documented by the occurrence of an irregular volume of sandy material (Fig. 3b). The alteration product is characterised by an increasing kaolinite content over smectite (sample TSC–36 of Scheiber and Viola, 2018). K–Ar dating on authigenic clays constrains alteration to the Cretaceous (127.4 ± 16.5 Ma, Table 1). Therefore, the age of faulting must be older than Cretaceous in age.

Outcrop S_3. The Goddo Fault Zone (GFZ) crops out along a road cut on the island of Goddo (northwestern Bømlo, Figs. 1b–4). The GFZ represents a E–dipping normal fault zone formed and reactivated during Permian–to–Cretaceous extensional tectonics (Viola et al., 2016; Fredin et al., 2017b; Scheiber and Viola, 2018). It is characterised by two separate and distinct fault cores (marked as S_{3A} and S_{3B} in Fig. 4a–b), separated and surrounded by highly fractured damage zones (Figs. 4a–b, 5a–b). The two fault cores consist of several brittle structural facies (*sensu* Tartaglia et al., 2020), i.e. different fault rocks characterised by different texture, mineralogical assemblages, and ages of formation (Viola et al., 2016). Brittle structural facies observed within the fault core include: (a) a polished PSS overlain by (b) a massive, well–sorted clay–rich gouge, (c) a phyllonitic gouge, and (d) a cohesive cataclasite (Fig. 5a–d). The PSS of the GFZ consists of a 1–2 cm-thick fine–grained quartz–coated polished surface, dipping 50°/070° and bearing dip–slip slickenlines (50°/070°)

associated with top–to–the–east normal fault steps (Fig. 5c–d). The overlying gouge core is 20–30 cm thick and it is composed of two main gouge layers showing different textures and age of formation (Viola et al., 2016). The clay–rich gouge consists of a 5–10 cm thick homogeneous and isotropic plastic gouge (Fig. 5c–d). The phyllonitic–gouge consists of a scaly, phyllosilicate–rich gouge containing a pervasive S–C' composite fabric (Fig. 5d). K–Ar illite dating showed that the phyllonitic gouge of the fault core S_{3B} developed during Permian extension (264.1 ± 5.4 Ma; Table 1); Triassic–Early Jurassic fault reactivation led to the formation of the clay–rich gouge and reworking of the phyllonitic gouge in the S_{3B} fault core (200.2 ± 4.1 Ma; Table 1) (Viola et al., 2016). The gouges are overlain by a 20–40 cm thick layer of indurated cataclasite, containing internal discrete shear planes decorated by purple–reddish–orange coatings of Fe–oxides (Fig. 5d). The occurrence of fault rocks is limited to the two described fault cores. The phyllonitic gouge is only observed in the S_{3B} fault core (Fig. 5d). No fault breccia bounding the fault core is observed.

The thickness of each fault core is in the order of 0.6–1 m (Fig. 5c–d), suggesting that each fault core may have accommodated a cumulative normal throw of 10–100 m (Torabi and Berg, 2011), thus defining a valuable example of a SRS fault zone (Viola et al., 2016). Accordingly, the damage zone width would be in the order of 10 to 100 m (Wilson et al., 2003; Faulkner et al., 2006, 2010). The damage zone is characterised by densely spaced (average spacing = 0.1–0.5 m) mesoscopic fractures related to both the background basement fracturing and to the GFZ itself (Scheiber and Viola, 2018). The GFZ damage zone is well exposed in the footwall, and between fault cores, whereas the geometry and exposure of the outcrop did not allow us to quantify the exact thickness of the hanging wall damage zone and the entire fault zone in the field (Fig. 4).

4.1.2 Group W – Weathered outcrops

Outcrop W_1. The outcrop is in the same locality of outcrop S_3–GFZ. The whole GFZ is crosscut by a series of poorly exposed alteration/weathering zones (outcrops marked with W_{1A}–W_{1B} in Fig. 4a; Fig. 6a–b). These weathering zones are spatially related to NNE–SSW, 1–2 m thick fracture corridors cutting across both the undeformed RGD host (Fig. 6a) and fault rocks (Fig. 6b) (Viola et al., 2016; Scheiber and Viola, 2018). The granodiorite within the fracture corridor mostly preserves its primary structure and cohesion at the hand specimen scale. Partially altered host rock lithons within the fracture corridor are embedded in a cohesionless granular matrix, mainly composed of quartz and clay minerals, which forms much less than 50 vol% of the altered outcrop (Fig. 6a–b). The mineralogical composition of the finest fraction of this matrix is dominated by smectite, as inferred from the sample BO–OFR–1 presented in Viola et al. (2016) and Fredin et al. (2017b). The weathering material included therein has been dated to the Early Cretaceous (125.2 ± 4.2 Ma, Table 1). The mineralogical composition and textural characteristics of the weathering products suggest that this outcrop is equivalent to the alteration facies A1 described by Riber et al. (2016).

Outcrop W_2. Outcrop W_2 is characterised by the occurrence of a pervasive NNW–SSE–trending fracture set (Fig. 6c). Fractures are preferentially organised in 1-m-thick clusters, separated by 2–5 m of non–fractured RGD host. Commonly, rock volumes within fracture clusters are heavily altered and transformed in a variably cohesive granular material preserving the magmatic fabric. Measurements were performed along a transect perpendicular to the main fracture trend, on a vertical surface and crossing through an alteration zone exhibiting a variable degree of weathering (from left to right in Fig. 6c). Qualitatively, the outcrop was subdivided into three main domains: (i) partially altered host granodiorite with some localised mesoscopic fractures (domain *d1* in Fig. 6c), (ii) granular cohesionless aggregate preserving the granodiorite fabric but no mesoscopic fractures (domain *d2* in Fig. 6c), (iii) granular aggregate with increasing clay content (domain *d3* in Fig. 6c), as inferred from plastic deformation of hand samples. Unpublished K–Ar illite dating data suggest that this alteration is older than Triassic and its mineralogical composition dominated by smectite (A. Margreth personal communication). As reported earlier, similar weathering characteristics have been observed in outcrop S_2.

Outcrop W_3. The outcrop is characterised by a 2 m thick altered rock volume within granodiorite, bounded by N–S trending fractures. The altered volume consists of a cohesionless granular aggregate, grading from saprock to mature, fine–grained clay–rich saprolite, enveloping variably altered "core stones" (i.e., remnant blocks of granodiorite less weathered than the embedding material and resulting from spheroidal weathering processes; cfr.Ryan et al., 2005; Fig. 6d) (Fredin et al., 2017b, 2017a). Weathering products in outcrop W_3 are well represented by the samples (Bomlo2–3–4) analysed by Fredin et al. (2017a,b), with a predominantly kaolinitic composition and likely developed during sub–aerial exposure of the crystalline basement in the Triassic (220–200 Ma, Table 1; Fredin et al., 2017b).

		XRD Data										K-Ar Dating		
Outcrop	**Sample ID**	**Grain Size (μm)**	Quartz	Kaolin	Illite/Mica 2M1	Illite/Mica 1M	Dioctahedral smectite	Interstratified illite/smectite	Albite/Anorthite	Anatase	Lepidocrocite	**Age (Ma)**	**Error (Ma)**	**Ref.**
S1	*TSC-1*	0.1 - 0.4		5			95		<1			**187.5**	**16.7**	[3]
		0.4 - 2	<1	9			87		4			192.6	13.7	
		2 - 6	1	18			75		6			260.4	8.1	
S2	*TSC-36*	<0.1		7			93					**127.4**	**16.5**	[3]
		0.1 - 0.4		25			75		<1	<1		177.6	16.2	
		0.4 - 2	<1	29	2		67		2	<1		261.7	8.4	
		2 - 6	<1	22	4		71		3	<1		324.0	9.0	
S3	*BO-GVI-1*	<0.1		1	20			79				**200.2**	**4.1**	[1]
		0.1 - 0.4		5	21		6	68				218.9	4.4	
		0.4 - 2	3	16	28		24	29		<1		240.7	5.0	
		2 - 6	34	8	14		13	30	1			272.1	5.5	
		6 - 10	35	8	17		12	27	1			282.9	5.7	
	BO-GVI-2	<0.1	<1	12	14	4	20	49	1			**264.1**	**5.4**	[1]
		0.1 - 0.4										262.0	5.3	
		0.4 - 2										303.8	6.3	
		2 - 6	2	9	32	2	16	35	4			349.6	7.1	
		6 - 10	2	9	33	4	17	31	4			354.4	7.1	
W1	*BO-OFR-1*	<0.1		7			93		<1			**125.2**	**4.2**	[1]
		0.1 - 0.4		7			93		<1			121.4	5.3	
		0.4 - 2		16			82		2			167.7	6.5	
		2 - 6	<1	22	3		71		3	<1		272.1	5.8	
		6 - 10	<1	25	2		68		4	1		287.5	6.2	
W3	*Bømlo 2*	<0.1					89				11	**210.0**	**13.1**	[2]
		0.1 - 0.4		4			78		2		16	290.2	10.6	
		0.4 - 2	<1	7			83		3		7	307.5	38.3	
		2 - 6	<1	8	6		79		3	<1	4	406.9	20.3	
	Bømlo 3	<2	<1	76	1		23					**217.3**	**4.8**	[2]
		2 - 6	<1	72	3		24							
	Bømlo 4	<2	<1	53			46		1			**233.0**	**5.0**	[2]
		2 - 6	<1	53	2		43		2					

Table 1. XRD data and K–Ar dates from synkinematic/authigenic illite samples of the outcrops studied in this paper. References: [1] Viola et al. (2016); [2] Fredin et al. (2017b); [3] Scheiber and Viola (2018).


a
S1
WNW
ESE
20 cm
b
S2
SE
NW
Fault core
PSS
Slickenlines
20 cm
S1
N=28
S2
N=4

487

488

Figure 3: (a) Fracture corridor at outcrop S_1. (b) The fault zone of outcrop S_2 is characterised by a thin, well–localised, gouge– and cataclasite–rich fault core enveloped by a 1 m thick, poorly–developed damage zone. Fluids percolating through the fault core led to the alteration of cataclasite and the damage zone observed in the central portion of the image. PSS: Principal Slip Surface. Stereonets: Lower hemisphere, equal area projection of fractures and fault planes. The black arrows represent the direction of movement of the hanging wall along the fault plane.

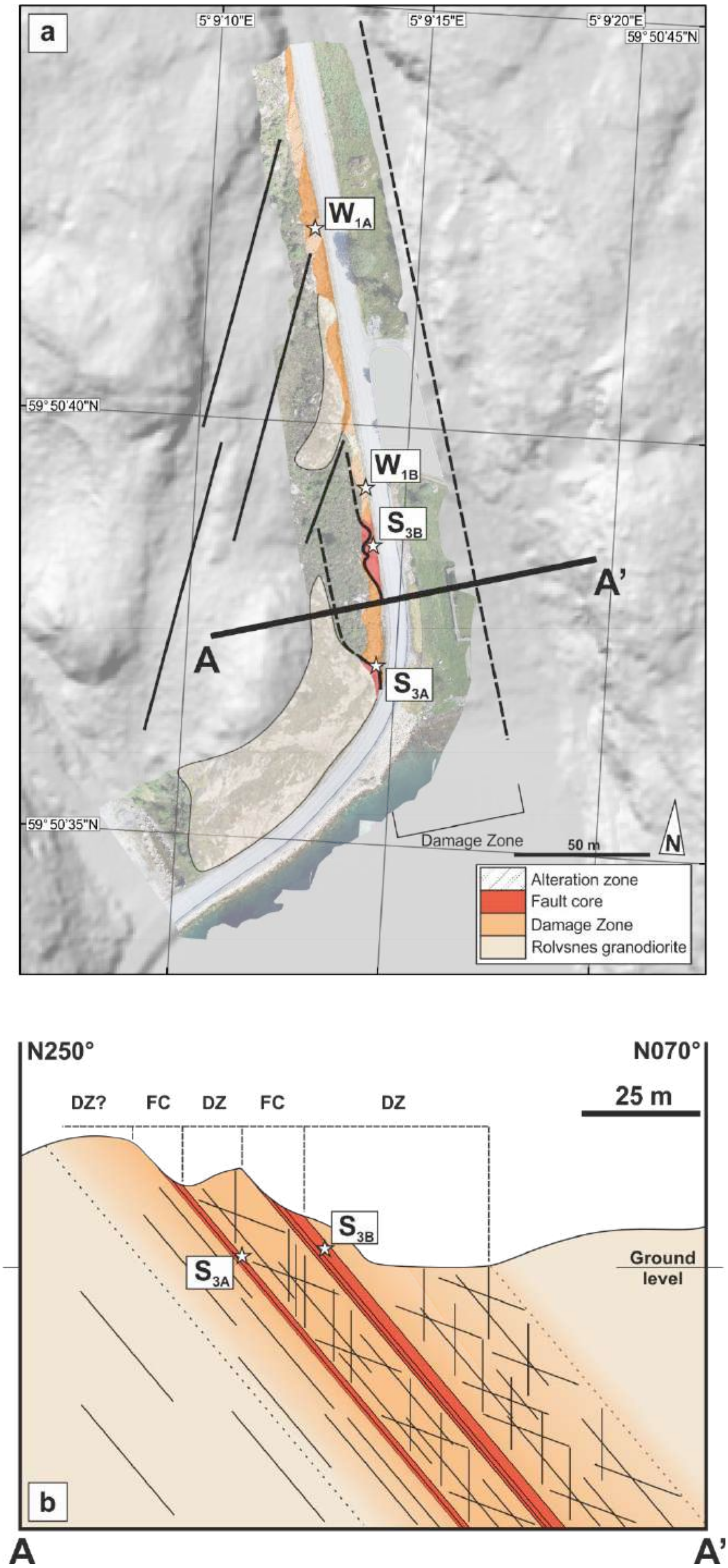
a
5°9'10"E
5°9'15"E
5°9'20"E
59°50'45"N
59°50'40"N
59°50'35"N
W1A
W1B
S3B
S3A
A
A'
Damage Zone
50 m
N
Alteration zone
Fault core
Damage Zone
Rolvsnes granodiorite
N250°
N070°
DZ?
FC
DZ
FC
DZ
25 m
Ground level
b
A
A'

495

Figure 4: (a) Schematic map of the Goddo Fault Zone (outcrop S_3) overlain on a composite UAV orthophoto and LiDAR digital elevation model image. The location of the studied outcrops along the fault zone (S_{3A}, S_{3B}, W_{1A}, W_{1B}) is also reported. Black thick lines represent fracture lineaments spatially related to discrete alteration zones. The black dashed lines bracket the supposed maximum width of the damage zone. (b) Geological cross section along the A–A’ profile of the Goddo Fault Zone. FC: Fault core; DZ: Damage zone.

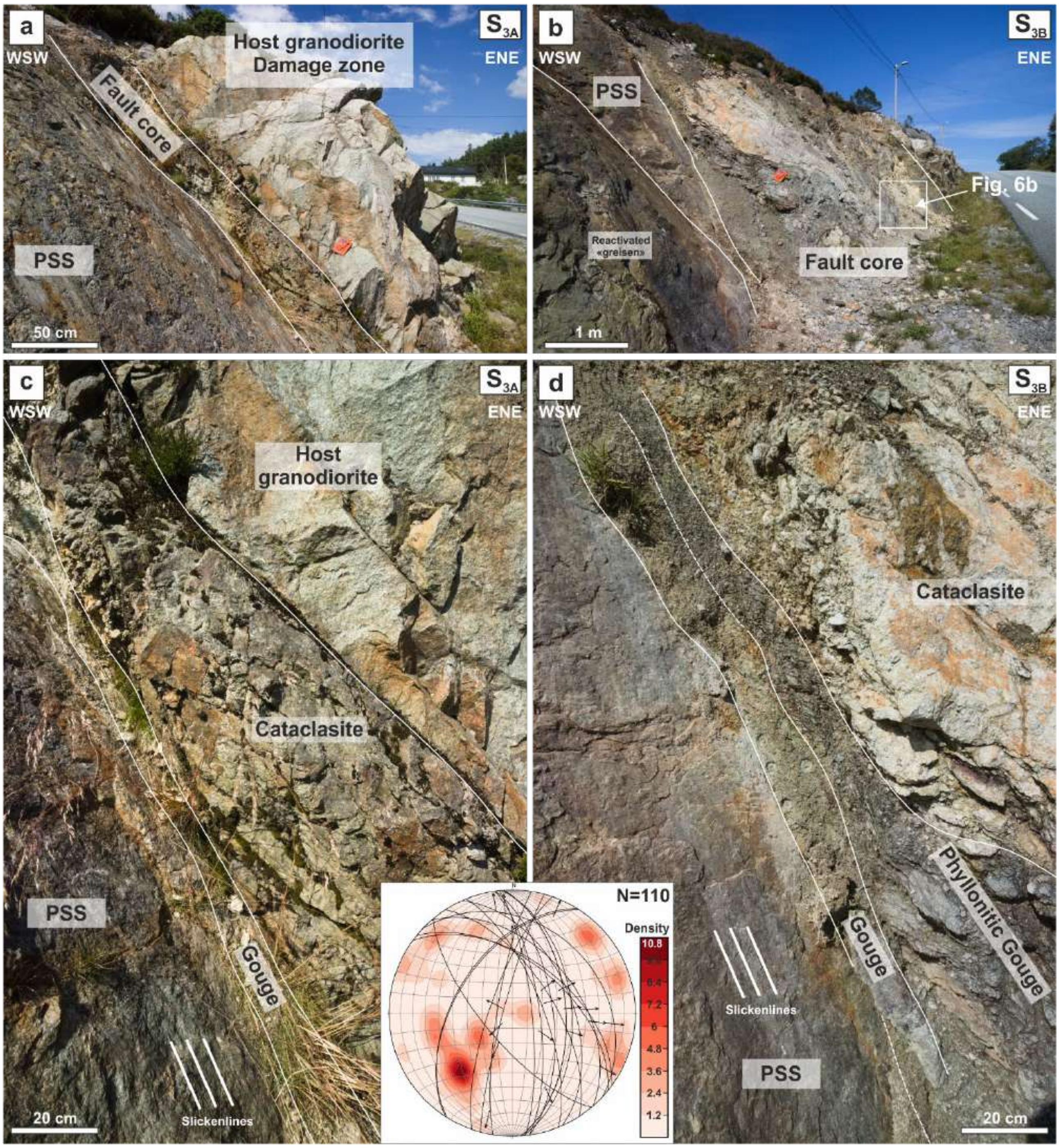

Figure 5: Representative outcrops of the Goddo Fault Zone. (a) Fault core at outcrop S_{3A}, showing the composite fault core. (b) Composite fault core and the reactivated slip surface of a "greisen" pre–faulting fracture exposed at S_{3B}. (c) Composite fault core at S_{3A}, showing the juxtaposition of cataclasite, gouges, and PSS. (d) Composite fault core at S_{3B}, showing the juxtaposition of cataclasite, gouge, and PSS. Note the alteration of the cataclasite layers. Stereonets: Lower hemisphere, equal area projection of fractures and fault planes at S_3. The whole dataset of fracture and fault planes

collected on the field is reported as contoured distribution of poles to fracture and fault planes (in red). Black great circle represent only those fracture and fault planes characterised by slip lines (lineations, slickenlines). The black arrows represent the direction of movement of the hanging wall along the fault plane.

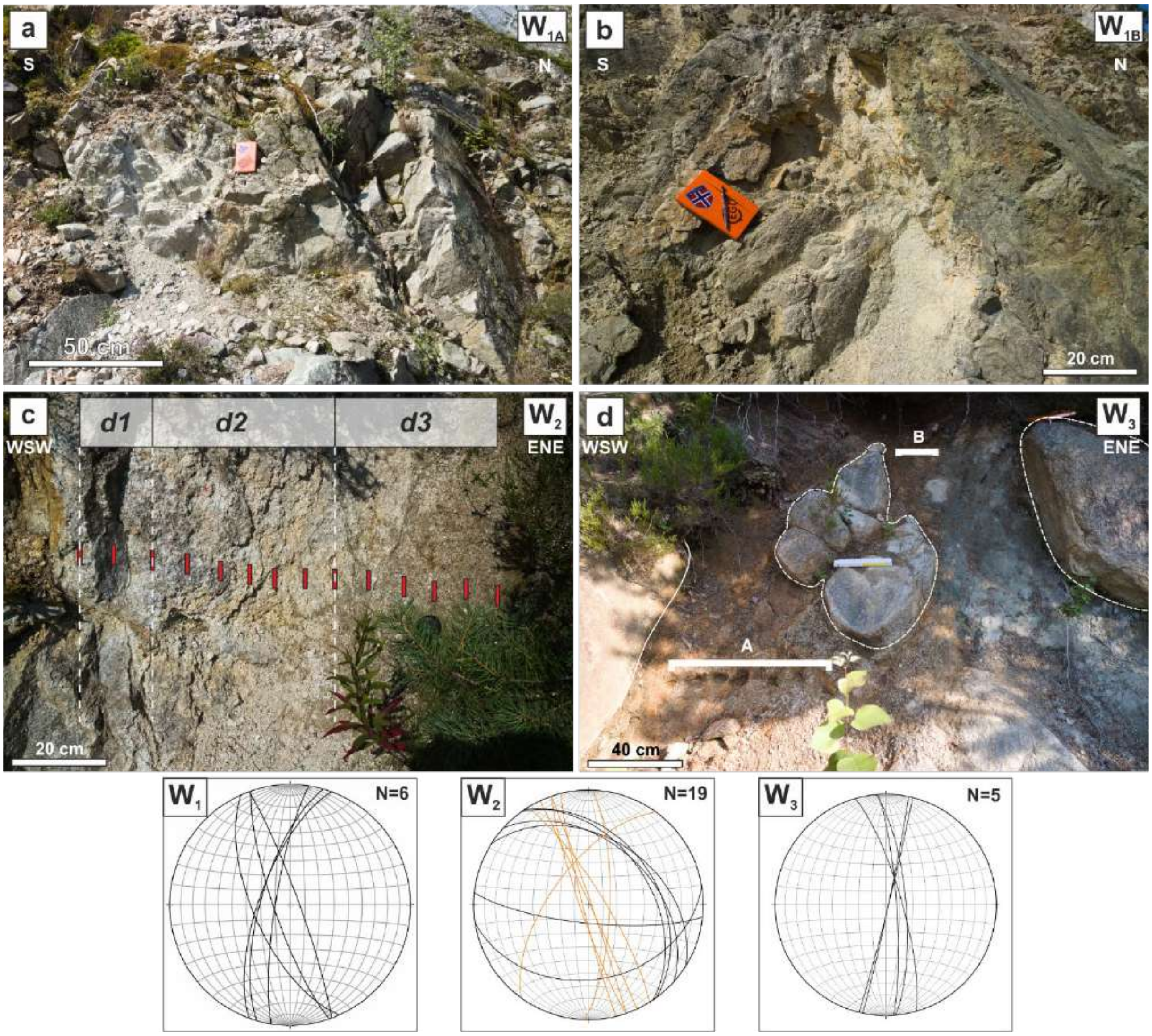

Figure 6: Representative outcrops of weathered granodiorite. (a) Alteration zone W_{1A} related to a NNE–SSW–trending fracture lineament. (b) Alteration of the host granodiorite within the damage zone of the GFZ at W_{1B} (detail of Fig. 5b). (c) Outcrop W_2 showing an increasing alteration profile along which we performed Schmidt hammer analysis and permeability measurements. (d) Outcrop W_3 (saprolite) showing relatively unaltered “core stones” (enclosed by dashed white lines). The thick white lines (A, B) represent the profile along which permeability and UCS measurements have been performed. Stereonets: Lower hemisphere, equal area projection of fracture planes at outcrops W_1, W_2 and W_3. Orientation of fractures within fracture clusters related to weathering zones at outcrop W_2 are highlighted in orange in the stereoplot.

4.2 UCS and permeability data

Data are presented in the following according to rock type (host rock, fault rocks and weathering products) as observed from many different outcrops, to derive an average value and constrain the natural variability range for each lithology. Average values of UCS and related standard deviations are reported in the text and Fig. 7a. Permeability ranges are presented in the text and data distributions are reported as boxplots in Fig. 7b.

4.2.1 Host rock

The RGD on the island of Bømlo still well preserves its magmatic texture and mineralogical composition. No pervasive ductile fabrics have been observed at the analysed outcrops, confirming the observations of Scheiber and Viola (2018). UCS values for the RGD host as observed at three different localities (outcrops S_1–S_2–W_3). Fresh, non–altered and non–mineralised granodiorite surfaces yield an average UCS value of 169 ± 36 MPa. Granodiorite surfaces bounding alteration/weathering zones (measured at outcrops W_2–W_3) exhibit a lower range of UCS variability, with an average value of 107 ± 29 MPa ("Weathered Granodiorite surface" in Fig. 7a). Results from permeability measurements on the pristine, non–fractured host granodiorite at different outcrops range between <10^{-4} D (below the actual reliability limit of the air–minipermeameter) and 0.1 D (Fig. 7b).

4.2.2 Outcrop S_1 – SSRS Fracture corridor

UCS measurements are from along a transect perpendicular to fracture strike. In order to evaluate the influence of fracture intensity on the UCS, we have quantified fracture intensity with circular scan windows (10 cm in diameter) centred on each measurement spot along the transect (Fig. 8a) (Watkins et al., 2015). UCS values comparable to fresh and slightly altered host RGD are measured in the outermost portion of the fracture corridor (Fig. 8b–c). Mechanical strength drastically decreases to 15–20 MPa toward the centre of the fracture corridor, where fracture intensity is higher (P_{21} = 74 m^{-}

^{1}; Fig. 8b–c, e). The permeability is inferred to be related to only meso–scale fracture aperture and interconnectivity. In order to have a relative comparison with the permeability data presented in the next sections, 2D structural permeability at the scale of the outcrop has been evaluated by analysing the digitised fracture network obtained from line drawing on a field photo of the core zone with the software FracPaQ (Healy et al., 2017). During line drawing, only the subvertical fractures were considered for the definition of the fracture network pattern (Fig. 8d). The subhorizontal fractures are likely related to post–tectonic outcrop modifications related to either post–glacial unloading or man–made excavation and blasting operations, given that such fracture orientation is not observed in any other fracture set related to the brittle deformation history of the Bømlo crystalline basement (Scheiber and Viola, 2018). The 2D permeability of the fracture pattern in the direction of flow was calculated considering a range of different values of fracture aperture, ranging from 0.01 to 1 mm and perfect connectivity among fractures. The outcrop–scale maximum permeability is always oriented parallel to the dominant subvertical fractures, and maximum values range between 10^{3} D to 10^{-3} D, for a fracture aperture of 1 mm and 0.01 mm, respectively (Fig. 8e).

4.2.3 Outcrops S_2–S_3 –Fault rocks

UCS bulk rock data on fault rocks have been measured at the S_2 and S_3 outcrops. The PSS is characterised by high UCS values when analysed normal to the surface (274 ± 32 MPa, Fig. 7a). Permeability measured normal to the slip surface is in the 0.05 to 0.06 D range (Fig. 7b). UCS of the clay–rich gouge layer is 12 ± 2 MPa, measured parallel to fault strike. Gouge layers present a lower range of permeability, between 10^{-3} D and 0.4 D measured parallel to fault strike (Fig. 7b). The rough exposure surface of the phyllonitic gouge facies did not allow us to perform reliable measurements (Fig. 5d). The cataclasite shows strongly anisotropic UCS, as inferred comparing the results obtained from measurements performed parallel (36 ± 22 MPa) and perpendicular (195 ± 37 MPa) to fault strike (Fig. 7a). The cataclastic core presents a variable permeability ranging between 10^{-3} D and 3 D when measured parallel to fault strike (Fig. 7b). The rough exposure surface of the cataclasite did not allow us to perform reliable measurements of permeability perpendicular to fault strike.

4.2.4 Group W_1–W_3. Weathering along fractures and fault zones

Outcrop W_1. UCS for altered granodiorite ranges between 30 and 90 MPa ("Weathered Granodiorite" in Fig. 7a). Values larger than 100 MPa are found in the weathered host granodiorite where the alteration is locally less developed. In the fracture corridor, altered granodiorite lithons are surrounded by a fine–grained sandy, rather non–cohesive matrix that exhibits low UCS values (<15 MPa) ("loose matrix" in Fig. 7a). The host granodiorite altered lithons exhibit a variable permeability, ranging between 10^{-3} D and 0.84 D (Fig. 7b).

Outcrop W_2. Outcrop W_2 displays a clear variation of mechanical strength and permeability with increasing weathering grade (Figs. 6c, 9a). Incipient alteration in domain *d1* exhibits variable UCS between 20 and 50 MPa and variable permeability ranging between 10^{-3} D and 1 D. Similar values were measured from the altered RGD observed at outcrop S_2. The cohesionless alteration products in domain *d2*, consisting of a grus–type sandy aggregate, yields UCS values <20 MPa. Permeability increases (from 0.1 D up to several Darcy's) and then decreases (from >1 D down to 0.01–0.1 D) moving from the left–hand side boundary to domain *d1* toward the right–hand side boundary to domain *d3* (Figs. 6c, 9a). Alteration domain *d3* is characterised by variable UCS < 20 MPa, and low permeability (from 0.01–0.1 D down to few mD).

Outcrop W_3. Partially weathered "core stones" exhibit a broad range of UCS values, ranging between 75 MPa and 125 MPa (Fig. 7a). They have a permeability included between 0.01 D and 0.1 D (Fig. 7b). The clay–rich saprolite volume has been analysed along two transects (Fig. 6d). Both transects yield almost constant UCS and permeability values within the clay–rich saprolite (UCS = 10–15 MPa, $k = 10^{-2}$–10^{-3} D) (Fig. 9b).

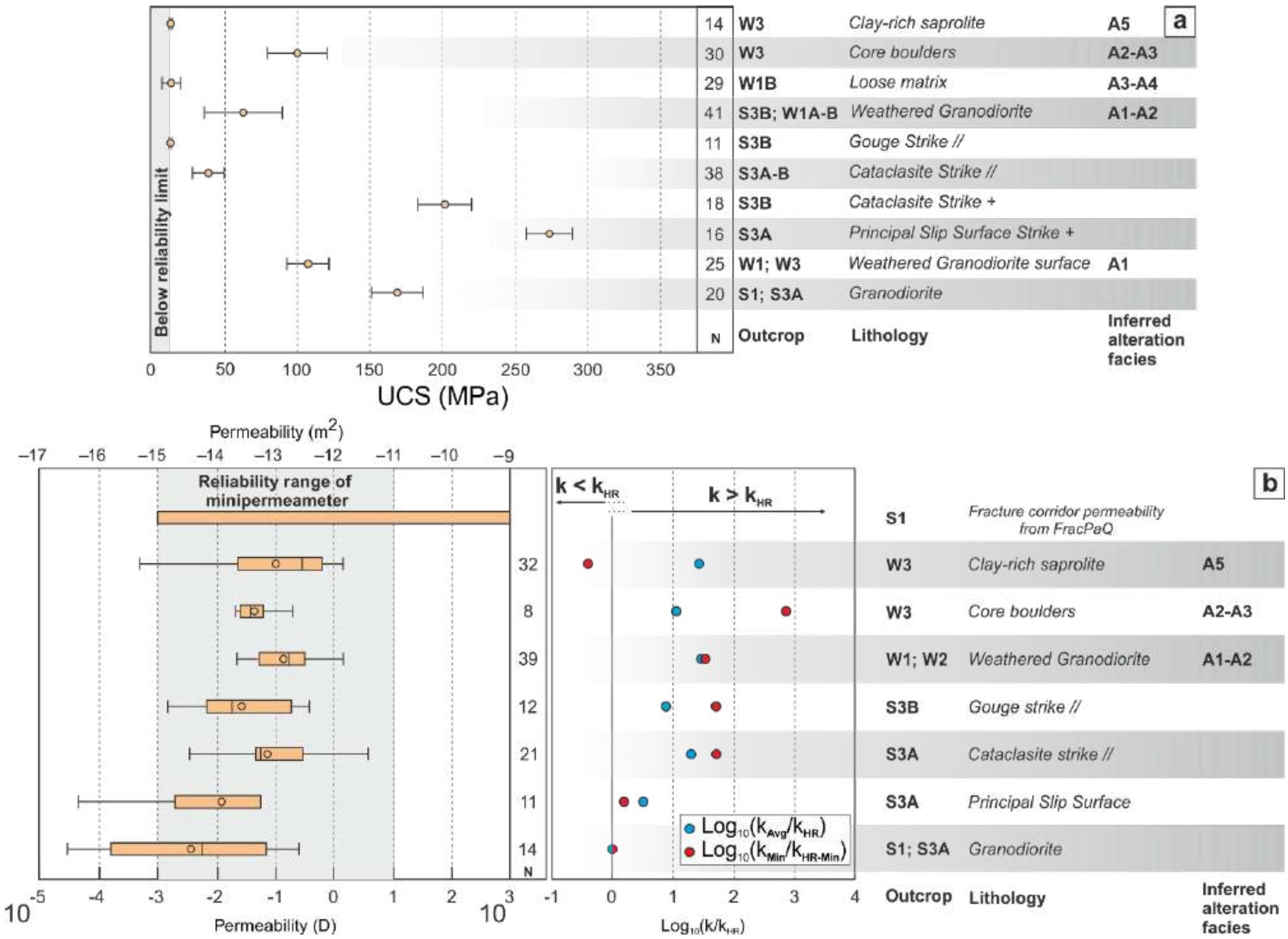

Figure 7: Mechanical strength and permeability box–plot diagrams. "Strike //" stands for data measured parallel to the fault plane. "Strike + " stands for data measured perpendicular to the fault plane. (a) Uniaxial Compressive Strength (UCS, MPa). For each analysed lithology we report the mean (orange dot), the standard deviation (1σ, black bars), the number of measurements (N), the outcrop(s) name on which the measurements were performed, and the corresponding alteration facies. (b) Permeability (m^2, D). The outcrop name and the corresponding alteration facies are reported. N: number of measurements for each lithology. Each box of the box–and–whiskers plot represents the range between the 1st and 3rd quartile of the distribution. The whole data range is represented by the extension of the whiskers. In (b) we also plot the logarithm of the permeability ratio ($Log_{10}(k/k_{HR})$) between the host rock and the selected lithology (Scibek, 2020). The ratio between mean values of permeability (blue dots) and the ratio between the minimum reported values (red dots) for each

lithology are also reported. It is worth noting that air–minipermeametry retrieved permeability values for saprolites are comparable to those obtained from laboratory measurements on saprolite samples from Bømlo and the Utsira High exploration wells (Lothe et al., 2018).

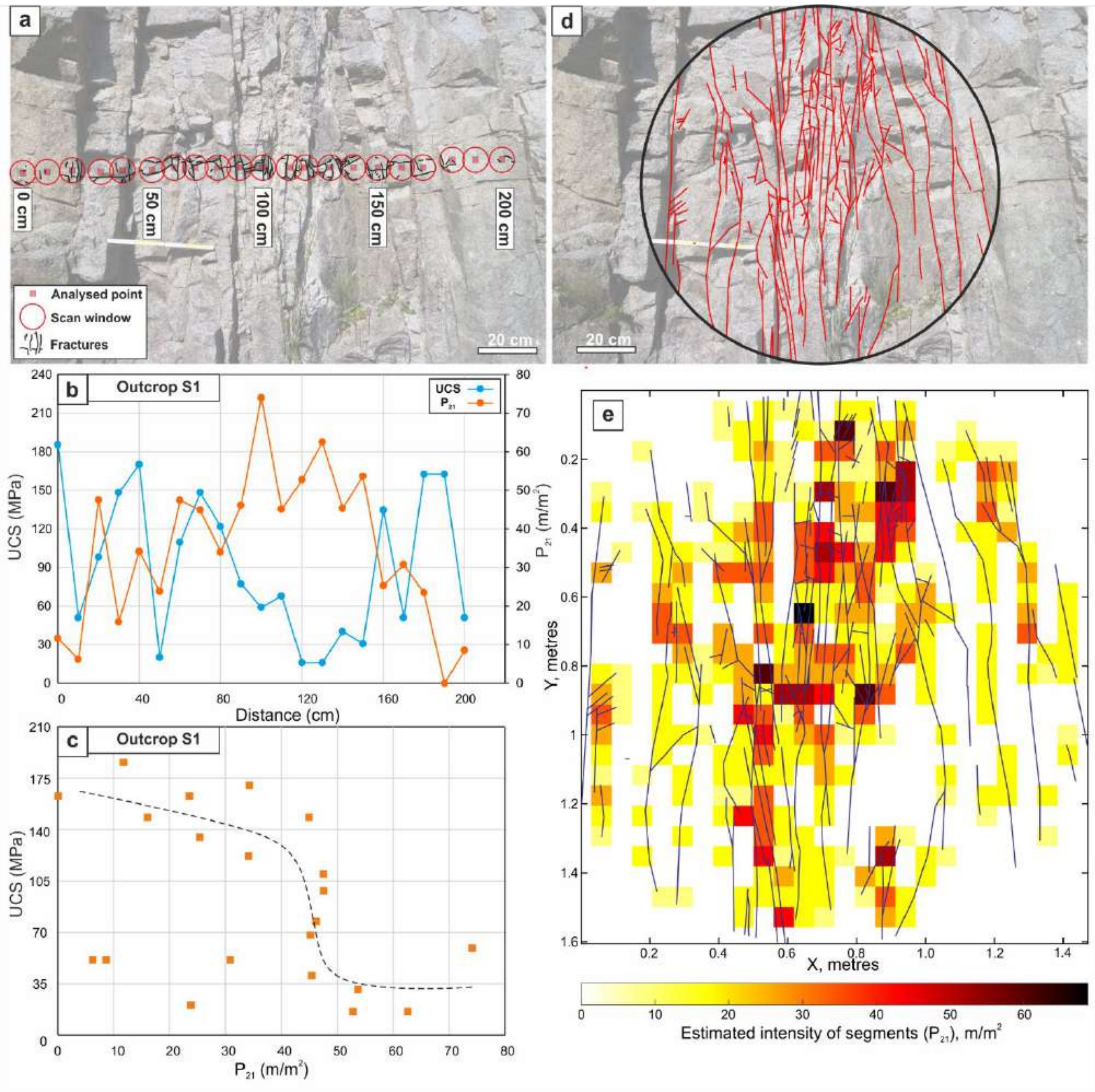

Figure 8: Results of the geomechanical and permeability measurements at outcrop S_1. (a) Location of the measurements for the Schmidt hammer analysis, and circular scan windows for fracture intensity P_{21} quantification; (b) Variation of mechanical strength (UCS) and fracture intensity (P_{21}) along the analysed transect. (c) UCS against fracture intensity P_{21}. Note the drastic decrease of mechanical strength after a threshold value of P_{21} at about 45 m^{-1}. (d) Line drawing of the subvertical fracture network analysed with FracPaQ (Healy et al., 2017); (e) Results of 2D permeability and fracture intensity quantification from FracPaQ..

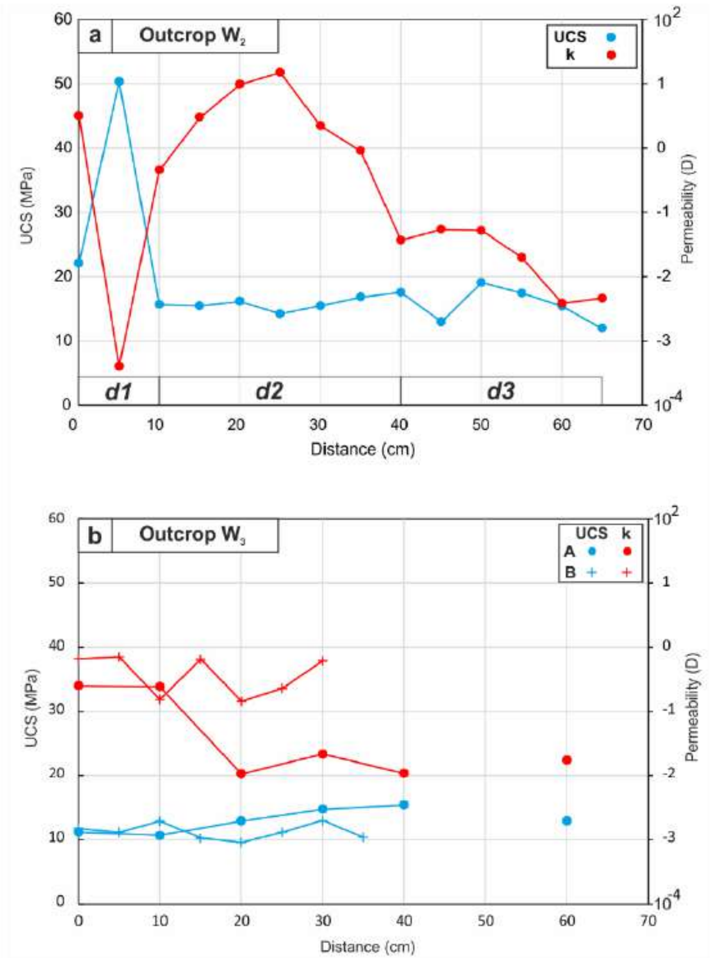

Figure 9: Results of mechanical strength and permeability quantification along the transect at outcrops (a) W_2 and (b) W_3. Letters A and B in (b) refer to the two transects shown in Fig. 6d.

5. **Discussion**

We have characterised the structural and weathering features controlling the matrix permeability and mechanical properties of the fractured and altered crystalline basement at a number of representative outcrops. In the following paragraphs we discuss (i) the host rock properties, (ii) the matrix permeability related to SSRS and SRS deformation zones, (iii) the mechanical strength and permeability related to weathering products, and (iv) their bearings on the definition of reservoir rock in crystalline basement structural highs.

The data presented in this paper represent the present–day, actual mechanical strength and permeability at surficial, ambient conditions. The extrapolation of these values to depth (at deeper structural levels or buried below a sedimentary cover) needs to take into consideration the effect of increasing confining pressure and temperature and the compaction processes (Rutqvist and Stephansson, 2003; Faulkner, 2004; Faulkner et al., 2006; Lothe et al., 2018). A further complication arises from the fact that the analysed onshore outcrops may have been affected by renewed alteration related to Cenozoic geomorphic and glaciogenic processes, which the fractured and weathered crystalline basement buried in the North Sea by the Mesozoic cover has, instead, probably escaped. The petrophysical and mechanical data presented here, however, are comparable (on average) with other results in the literature from standardised laboratory tests on fresh samples from onshore outcrops and offshore core samples of the same rock types analysed here (Lothe et al., 2018; Walter et al., 2018; Høien et al., 2019). This suggests that possible Cenozoic geomorphic and glaciogenic processes have only slightly affected the textural, mechanical and petrophysical characteristics of the studied onshore outcrops.

5.1 Host rock properties

The observed host granodiorite UCS is comparable to the reference values reported in the database by SINTEF for Norwegian rock types (Høien et al., 2019). Permeability data from the RGD are quite different from available laboratory permeability measurements on intact rocks (Sibson and Rowland, 2003). Most of the host rock permeability values are comparable with permeability values obtained from fractured crystalline and igneous rock in fault damage zones (Forster and Evans, 1991; Evans et al., 1997; Cappa and Rutqvist, 2011; Gomila et al., 2016). This discrepancy might be related to either: (i) an analytical error during measurement (i.e. air slippage from the non–perfectly sealed contact between the probe tip and the rough surface); (ii) enhanced permeability related to the increased microfracture density in the proximity of fracture and fault zones (Mitchell and Faulkner, 2012; Belaidi et al., 2018; Torabi et al., 2018; Staněk and Géraud, 2019); (iii) enhanced permeability related to recent, very local surficial weathering processes. Therefore, further investigations are needed to properly constrain the permeability of the host RGD.

5.2 Group S –Mechanical strength and permeability of deformation zones

The host crystalline basement (RGD) is overprinted by several sets of fractures, including fracture corridors and SSRS–SRS fault zones (Gabrielsen and Braathen, 2014; Scheiber and Viola, 2018). These fracture lineaments affect differently the mechanical and permeability properties of the host RGD and thus require a separate discussion.

5.2.1 SSRS fracture corridors

Fracture corridors are characterised by high–fracture–intensity deformation zones, accommodating limited (< 1m) throw, mostly barren of fault rock. The outcrop mechanical strength and bulk permeability are mainly controlled by the spatial distribution of meso–scale fractures (Fig. 8c, e).The increase in local fracture intensity leads to a drastic decrease of the host rock mechanical strength for P_{21} > 40–50 m/m^2 (Fig. 8b–c). High fracture intensity leads to a significant increase of fracture permeability up to 1–10^3 D (Fig. 7b). The largest 2D permeability in the direction of flow is observed parallel to the longer, subvertical and well interconnected fractures (Fig. 8e). Such a fracture network represents a preferential pathway for fluid flow (Souque et al., 2019). Thus, the permeability of limited–throw SSRS fracture corridors is controlled by the mesoscopic fracture porosity. On the other hand, microscopic fracture porosity may contribute to the matrix mechanical strength and permeability to only a very limited extent (Faulkner et al., 2006; Mitchell and Faulkner, 2012; Rempe et al., 2018). A local increase in permeability related to microscopic fracture porosity is reported by Torabi et al. (2018) for fracture corridors developed within the Øygarden Gneiss Complex in the Bergen area. Therefore, such SSRS, limited–throw fractures remarkably affect both the overall mechanical and permeability properties of the crystalline basement.

5.2.2 SSRS and SRS fault cores

Strain accommodation and development of fault rocks along SSRS–SRS fault zones resulted in a drastic modification of textural, mechanical and petrophysical properties of the host RGD. Fault zones, either SSRS or SRS, are characterised by the development of a variably thick fault core, defined by the occurrence of fault rocks, and a variably developed damage zone (Caine et al., 1996). SSRS fault cores are likely to be characterised by thin, single fault cores (< 1m thickness) surrounded by poorly developed damage zones (e.g., outcrop S_2). SRS fault zones, instead, may be characterised by the occurrence of thicker (≥ 1 m), multi–strand fault cores surrounded by complex, thick and high–fracture–intensity damage zones (Walsh et al., 1999; Gabrielsen and Braathen, 2014).

In both SSRS and SRS fault zones, the fault core is characterised by a composite fault plane–parallel sequence of fault rocks including a PSS, cataclasite, and potentially (several) gouge layers. Extreme strain localisation and rock comminution resulted in the formation of a thin, yet mechanically strong, PSS with a low permeability (Fig. 7a,b). Cataclasite mechanical strength is strongly anisotropic (Fig. 7a). Cataclasites are stronger (UCS >> 100 MPa) where measured normal to the fault plane and weaker (UCS <50 MPa) where measured parallel to the fault plane. Cataclasite permeability is up to two orders of magnitude larger than the average permeability of the host rock (Fig. 7b). Gouge layers yield a very–low mechanical strength (UCS < 20 MPa), and low permeability parallel to the fault plane ($k < 10^{-1}$ D). A strong anisotropy in permeability is expected for both cataclasite and gouge layers (up to three orders of magnitude) (Faulkner and Rutter, 1998). The lower strength and increased permeability parallel to the fault plane is probably also related to a higher density of fault–parallel microfractures and micro–shear planes within cataclasite and gouge layers (Zhang and Tullis, 1998). A pervasive phyllosilicate–bearing foliation characterises the phyllonitic gouge of the GFZ. Thus, even though we lack direct measurements, a strong permeability and strength anisotropy should be expected for the phyllonitic gouge (Shea and Kronenberg, 1993; Niemeijer and Spiers, 2005; Leclère et al., 2015). Cataclasites and gouge layers are in any case two orders of magnitude more permeable that the host RGD (Fig. 7b). Grain–size reduction, cataclasis and microfracturing processes likely led to the increased micro–fracture–related porosity of fault rocks with respect to that of the host granodiorite (Staněk and Géraud, 2019).

5.2.3 Damage zones

The discrete and multi–strand fault cores are surrounded by variably developed fracture–dominated damage zones, whose width is one order of magnitude larger than fault core thickness (Faulkner et al., 2010). The mechanical strength and bulk permeability of the damage zone is strictly dependent on the intensity, mechanical properties and geometry of multi–scale fractures related to both the fault zone and the basement background fracturing (Bruhn et al., 1994; Faulkner et al., 2006; Gudmundsson et al., 2010; Mitchell and Faulkner, 2012; Rempe et al., 2018). Local permeability within the damage zone might be as large as the permeability of similarly high–fracture–intensity fracture corridors (Gabrielsen and Braathen, 2014). An accurate characterisation of the fracture pattern geometry is needed to properly quantify the effect of mesoscopic fractures on the evolution of mechanical properties and bulk permeability in a damage zone (Healy, 2008; Gudmundsson et al., 2010).

In conclusion, SSRS and SRS deformation zones have distinctive structural characteristics controlling their permeability structure. Low–strain, low–displacement SSRS fracture corridors characterised by open, non–mineralised fractures greatly enhance the permeability of the crystalline basement at the sub–seismic–resolution scale. They form very localised, narrow (1–10 m in width) highly–efficient conduits for fluid flow. The largest permeability is observed parallel to the average fracture plane orientation. SSRS and SRS fault zones are characterised by two domains with characteristic permeability (Caine et al., 1996; Evans et al., 1997): (i) the fault core, including low–permeability fault rocks; (ii) the damage zone, defined by a high–permeability multiscale fracture network. The permeability of fault rocks and damage zones is in any case several orders of magnitude larger than the host rock. Therefore, despite their effective (SSRS or SRS) or relative (fault core/damage zone width ratio) size characteristics, fault zones developed within the granodioritic crystalline basement of Bømlo are likely to act invariably as preferential conduits for fluid flow. Fluid flow will be promoted in any directions parallel to the fault zone, along the highly fractured damage zones. Fluid flow from footwall to hanging wall of SRS fault zones, or vice versa, might be buffered/limited by the occurrence of relatively low–permeability fault cores.

5.3 Group W outcrops and a comparison with the Utsira High weathering profile

Several authors described in detail the mineralogical and textural changes of the granitoid crystalline basement of the Utsira High related to the development of a saprolitic weathering profile identified in the core samples of offshore exploratory wells (Riber et al., 2015, 2016, 2017, 2019a; Lothe et al., 2018). They describe five different alteration facies accounting for the observed gradual disaggregation of the igneous host rock, the alteration of feldspar, and clay mineral formation. In their model, progressive downward penetration of meteoric fluids from the top–basement surface led to the development of a thick weathering profile containing both saprock and more mature saprolite formed at the expense of the host granitoid (Fig. 2a–b) (Riber et al., 2015, 2019b; Walter et al., 2018; Zauyah et al., 2018). Weathering extends from the top–basement surface (that was exposed to a sub–aerial tropical–humid climate) into depth in the rock column: the progressive degradation of the host rock primary structure and the presence of a pervasive network of fractures and fault zones promoted the penetration at depth of fluids enhancing alteration (Braathen et al., 2018; Walter et al., 2018; Zauyah et al., 2018). The weathering process induces specific textural and mineralogical modification of the host rock. Incipient weathering along fractures leads to discolouring and limited mineral alteration while still preserving the igneous/metamorphic rock texture ("altered coherent facies A1–A2" in Riber et al., 2016; Fig. 2b). The alteration of biotite and plagioclase leads to progressive grain disaggregation and grain fracturing, clay mineral and Al–Fe oxide formation (saprock – saprolite, "altered incoherent facies A3–A5" in Riber et al., 2016; Fig. 2b) (Goodfellow et al., 2016; Hayes et al., 2019). Progressive weathering is also reflected in a varying mineralogy of authigenic clay minerals, with smectite being progressively substituted by kaolinite as the degree of weathering increases (Coggan et al., 2013; Riber et al., 2016).

A similar transition in mineralogical and textural characteristics of the RGD with increasing alteration can be deduced by the comparison of the preserved weathering remnants at the analysed Group W outcrops. Each outcrop effectively shows different textural, mineralogical (clay–mineral amounts and species), and mechanical characteristics, which indicate progressive weathering and alteration. Outcrops W_1–S_1 only display partial alteration of the wall rock along fractures while preserving the textural and mechanical properties of the host rock. The weathering products are represented by samples BO–OFR–1 (Viola et al., 2016) and TSC–1 (Scheiber and Viola, 2018). The finest–fractions of these samples are enriched in smectite–like phases, suggesting only incipient alteration (Coggan et al., 2013; Riber et al., 2016). The characteristics of this outcrop, thus, resemble those of the "alteration facies A1–A2" described by Riber et al. (2016). The alteration products observed at outcrop W_2 document, instead, a transition from a coherent host rock (domain *d1* in Fig. 6c) toward a cohesionless, sandy, grus–type aggregate preserving the magmatic texture but not the mechanical cohesion of the host rock and increasing clay content (domain *d3* in Fig. 6c). The intermediate alteration domain *d2* at outcrop W_2 presents textural and mechanical characteristics similar to the alteration products observed at outcrop S_2. Sample TSC–36 from outcrop S_2 shows increasing kaolinite content over smectite (Scheiber and Viola, 2018). The clay content and the textural characteristics of domain *d2* at outcrop W_2 and outcrop S_2 are similar to those described for "alteration facies A3–A4" by Riber et al. (2016). The clay–rich alteration product in outcrop W_3 is present in the set of samples analysed by Fredin et al. (2017b) (Bomlo2–3–4). Kaolinite is predominant over smectite–like phases, suggesting an advanced stage of alteration (Coggan et al., 2013; Riber et al., 2016). Outcrop W_3 mineralogical and textural characteristics are similar to the "alteration facies A5" described by Riber et al. (2016).

Even though the alteration products analysed in the Group W outcrops may result from diachronic events, they all present textural and mineralogical characteristics which are ascribable to kaolinitisation and/or saprolitisation of the RGD host (Coggan et al., 2013; Riber et al., 2016; Fredin et al., 2017b). Indeed, alteration processes took place at either shallow crustal levels (<6km? depth, Scheiber and Viola, 2018) or surficial conditions (weathering – saprolitisation) (Fredin et al., 2017b). It is worth noting that, in each of the analysed outcrops, the weathering products postdate the formation of brittle structures and are not overprinted by any subsequent brittle deformation. This may suggest that weathering likely developed during periods of quiescent tectonic activity, as it is postulated for the development of thick saprolitic horizons (Fredin et al., 2017b)

Therefore, we speculate that the studied Group W outcrops may be adopted as representative of the different stages of progressive weathering. The partially altered outcrop W_1 represents the deepest portions of the weathering profile; the outcrop W_2 represents the intermediate alteration stage and the transition toward more evolved alteration products, which are well represented by outcrop W_3 (Fig. 10) (Lothe et al., 2018).

Such a defined weathering profile displays a progressive degradation of mechanical strength and an overall permeability enhancement with the increasing weathering grade (from A1 to A5, Fig. 10b). Incipient alteration A1–A2 leads, on average, to a progressive decrease in mechanical strength of about 50% of the intact RGD. The permeability at this stage of weathering is increased up to 0.01–1 D. The transition from coherent (A2) to incoherent alteration facies (A3–A5) is characterised by a drastic decrease in mechanical strength (UCS down to < 20 MPa, Fig. 10b). Conversely, the permeability increases up to 10 D within alteration facies A3–A4, and then progressively decreases toward 10^{-4} D when approaching alteration facies A5 (Fig. 10b).

The observed variability of the studied properties through the weathering profile is similar to that commonly reported from saprolitic profiles and alteration profiles related to granite kaolinitisation (Coggan et al., 2013; Lothe et al., 2018; Walter et al., 2018). In such contexts, the variation of mechanical strength and permeability are commonly related to the development and evolution of micro–porosity with increasing weathering (Goodfellow et al., 2016; Lothe et al., 2018; Walter et al., 2018; Hayes et al., 2019). Microstructural investigations suggest that the petrophysical properties of incipient alteration stages (coherent alteration facies A1–A2) are controlled by microfracture–related porosity and biotite alteration (Goodfellow et al., 2016; Walter et al., 2018). The increasing alteration of biotite and plagioclase into clay–minerals (alteration facies A3–A4) promotes the development of vacuole–shaped porosity and triggers micro–fracturing as a consequence of positive volume changes caused by the oxidation reactions in the altering rock (Goodfellow et al., 2016; Walter et al., 2018). At this stage, highly interconnected pores and micro–fractures enhance the effective permeability and storage capacity of the weathered rock (Walter et al., 2018). Accordingly, increased micro–porosity and progressive clay–mineral formation lead to the observed drastic decrease in mechanical strength between cohesive and cohesionless alteration facies, similarly to what reported by Coggan et al. (2013) during progressive granite kaolinitisation. The most advanced stages of weathering (alteration facies A5) are characterised by the complete alteration of biotite and plagioclase into clay–minerals and Fe–oxides. At this stage, mineral alteration and neoblastesis lead to obstruction of the previously developed micro–porosity and to the observed reduction of permeability (Walter et al., 2018). As a result, weathering leads to immediate and drastic decrease of mechanical strength, whereas permeability firstly increases and then decreases during weathering process progression (Fig. 10).

The characteristics of the weathering profile studied here have three main important implications for the characterization of reservoir rocks buried offshore beneath the sedimentary cover in the North Sea structural highs.

(i) Weathering around fracture zones, progressive matrix disaggregation, homogenization, and the resulting blurring of the structural discontinuities drive the transition from structurally controlled permeability of the intact host rock toward the matrix–controlled permeability of intermediate alteration facies (Fig. 10). Fracture zones are characterised by high permeability, which is, however, spatially confined to the mesoscopic fracture porosity and fracture aperture. The highly permeable alteration facies A3 is two orders of magnitude less permeable than the maximum permeability inferred for fracture corridors (with a fracture aperture of 1 mm). However, it involves larger volumes of the host rock, and thus dramatically increases the storage capacity of the reservoir rocks.

(ii) The low permeability of alteration facies A5 (saprolite) suggests that the top layers of the weathering profile, when preserved, may act as a partial seal to fluid flow at the base of the sedimentary cover atop the basement structural highs (Dewandel et al., 2006; Walter et al., 2018).

(iii) The analysed paleo–weathering profile developed during the Mesozoic, and was then buried below the Jurassic–Cretaceous sedimentary succession of the central North Sea. The observed differential mechanical strength may have led to different compaction patterns and behaviours, and thus a differential modification of the permeability of weathering products during the burial history of the paleo–weathering profile (Lothe et al., 2018). The weaker clay–rich saprolites may have undergone to a significant change of the original secondary porosity and permeability when compared to the more stiff, granular saprock and incipient alteration facies (Lothe et al., 2018; Walter et al., 2018).

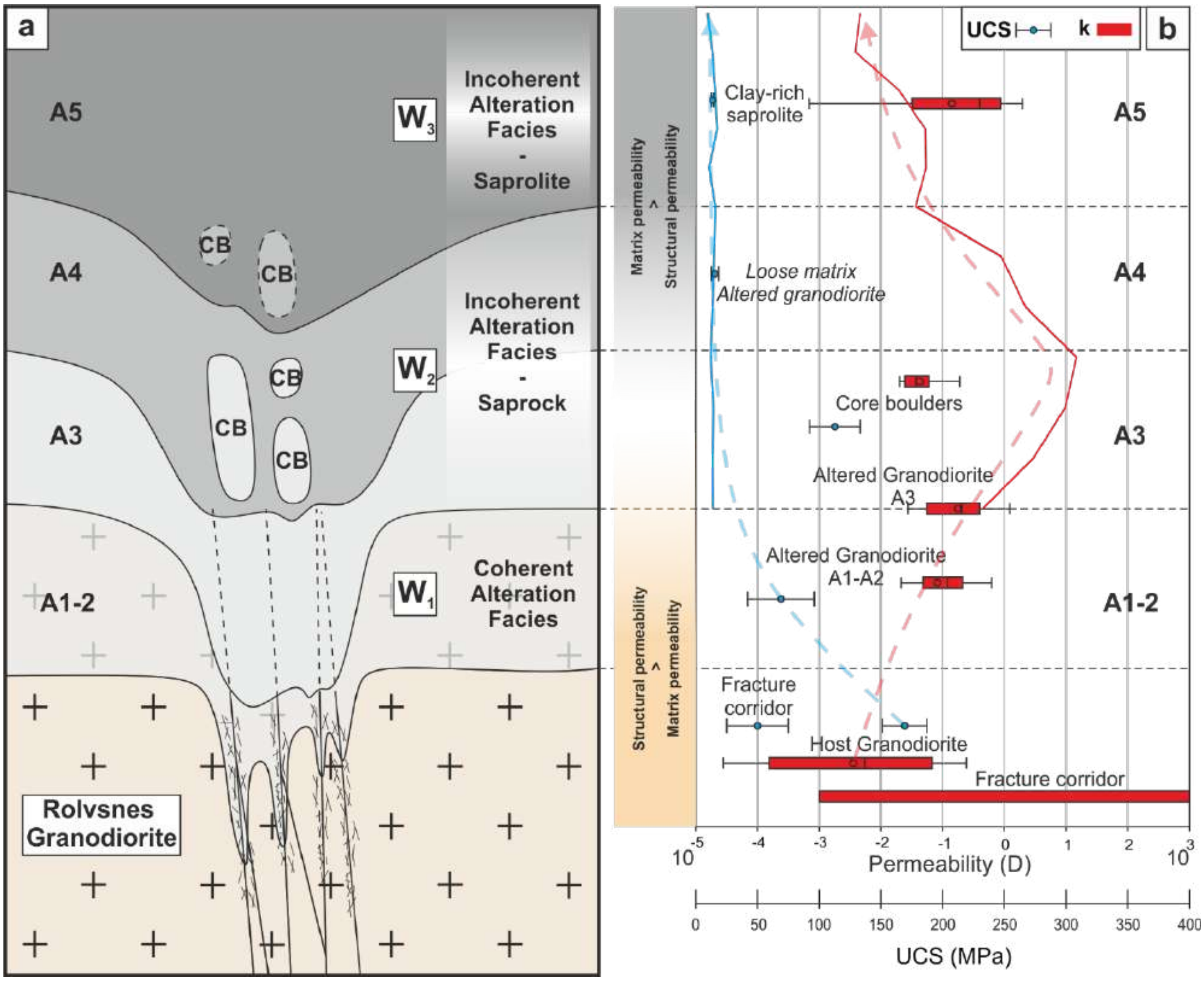

Figure 10: (a) Schematic representation of the top–basement weathering profile. The penetration of weathering processes into the crystalline basement is promoted by the structural discontinuities, such as SSRS fractures and fault zones. Alteration intensity decreases with depth. With increasing alteration, structural permeability is progressively replaced by matrix permeability related to the alteration products. (b) Mechanical strength and permeability variations through the alteration profile. The continuous red and light blue curves represent the mechanical strength and permeability observed at W_2. The dashed red and blue curves represent the overall general trend of variation of k and UCS, respectively, through the weathering profile. An initial permeability increment in the deepest portion of the alteration profile is superseded by a drastic permeability decrement toward the more evolved weathering stages.

5.4 Reservoir rocks in fractured and weathered basement

The reservoir rocks in fractured and weathered crystalline basement are made up of (Braathen et al., 2018): (1) the fractures and fault (damage) zones within the non–weathered crystalline basement, in which permeability is structurally controlled (Figs. 11, 12), and (2) the products of weathering and alteration, such as the overlying top–basement paleo–weathering profile where the permeability is dominated by the matrix properties of the weathered products (Figs. 10, 12).

The crystalline basement is characterised by the occurrence of a complex network of variably oriented brittle deformation zones (Gabrielsen and Braathen, 2014; Scheiber and Viola, 2018). Fracture corridors and damage zones related to both SSRS and SRS fault zones represent high–permeability conduits for fluid flow (Fig. 11a). The volume of the fractured reservoir suited for fluid storage is therefore limited to the overall deformation zone volume. However, the occurrence of fault rocks within SSRS and SRS fault cores may limit the migration of fluids between highly permeable footwall and hanging wall damage zones. In addition, the intersection of variably oriented fault zones may limit the overall lateral fluid flow through the large–scale network of SSRS–SRS fracture lineaments. This would lead to the formation of fault bounded polyhedral domains (i.e. "reservoir compartments") of the fractured crystalline basement (Fig. 11b) (Watkins et al., 2018). Within each domain, fluid flow is limited to the high permeability fracture corridors and footwall/hanging wall damage zone connected to the domain bounding faults (Fig. 11b).

The reservoir storage volume is likely increased within the top–basement weathering profile and fracture–related alteration zones. Weathering may lead to the formation of very thick (up to 100 meter thick) profiles characterised by high porosity and permeability (Braathen et al., 2018; Walter et al., 2018) (Fig. 12). In addition, fluid percolation through fracture zones may lead to the deep penetration of weathering processes, down to even 300 m below the top–basement paleo surface (Place et al., 2016; Walter et al., 2018). Furthermore, the most altered A5 facies may represent a top–seal layer to the underlying weathered and fractured basement high, buffering the upward migration of fluids toward the overlying sedimentary succession (Figs. 10, 12) (Walter et al., 2018).

5.5 Mechanical strength of fractured and weathered crystalline basement

The fractured and weathered unconventional reservoir under consideration is thus composed of several structural and textural elements with strikingly different mechanical strength. The fracture network and the spatial distribution of weathering/alteration products lead to a significant mechanical heterogeneity/anisotropy within the crystalline basement. In turn, this mechanical heterogeneity and anisotropy may in places significantly perturb the regional stress field (Gudmundsson et al., 2010). This could lead to the relevant modification of the overall fracture network geometry, fracture orientation and spacing within the mechanically heterogeneous rock volume during both natural deformation and induced fracturing of the reservoir (Jeanne et al., 2013; Smart et al., 2014). The occurrence of mechanically weak layers, such as the top–basement weathering profile, the gouge–bearing fault cores, and the partially altered fracture corridors within the crystalline basement may control the orientation and propagation of natural or induced fractures during either tectonic deformation or reservoir production (Douma et al., 2019; Forbes Inskip et al., 2020). In particular, the occurrence of these low–mechanical strength layers and localised heterogeneities may arrest the propagation of fractures artificially induced during the exploitation phase of unconventional reservoirs to enhance the local structural permeability of the host low–permeability crystalline rocks and stimulate production (Forbes Inskip et al., 2020).

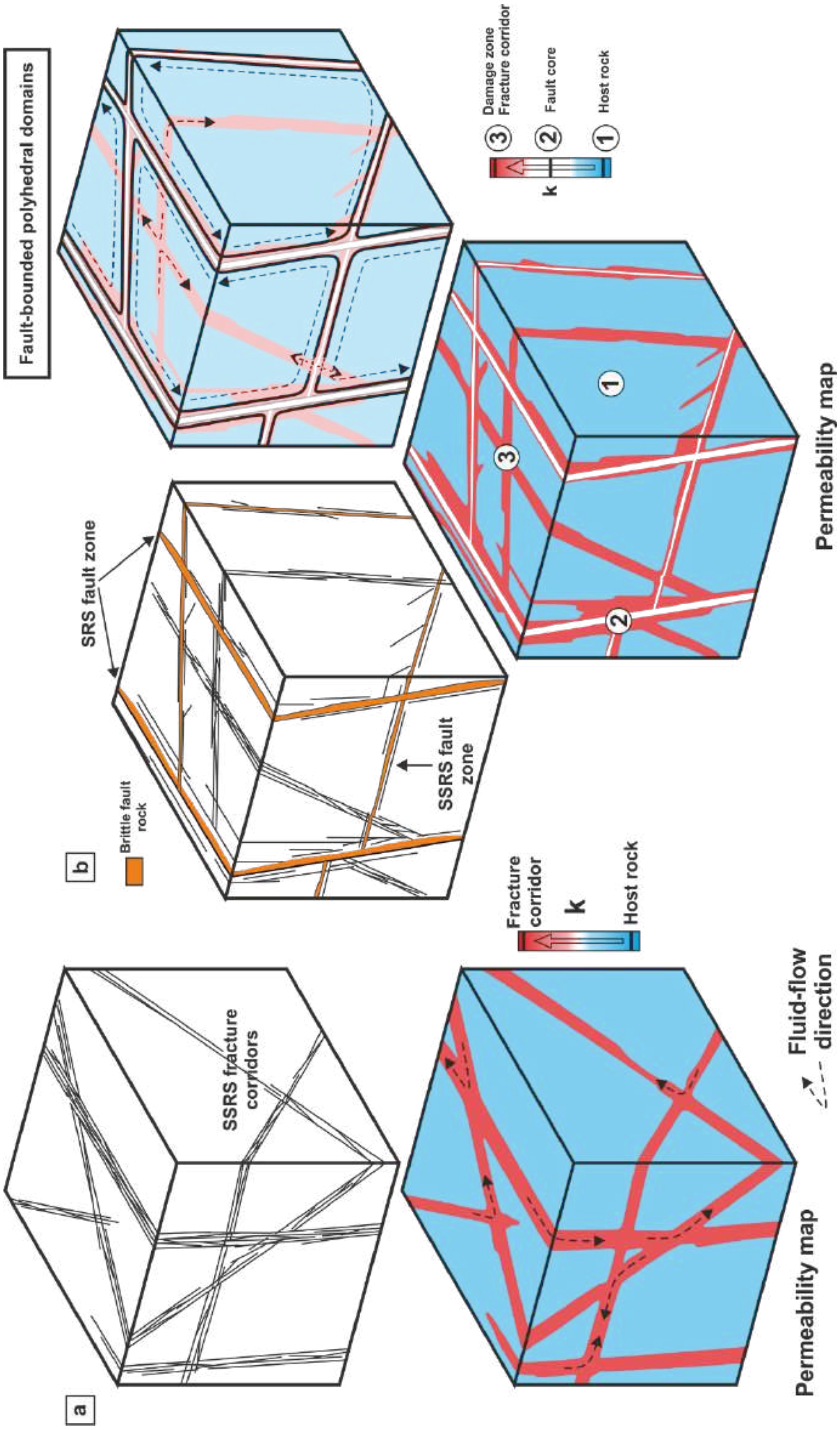

Figure 11: Schematic representation of the conceptualised fractured basement reservoir. (a) Low–strain fracture corridors lead to the development of a high–permeability network of fracture lineaments, dominated by the structural permeability. The randomly oriented dashed arrows in the coloured permeability map indicate the lack of reservoir compartmentalization. (b) The development

of sub–seismic–resolution scale (SSRS) and seismic–resolution scale (SRS) fault zones, and related fault rocks within fault cores lead to the development of local low–permeability barriers to fluid flow. The large–scale fracture network is then “compartmentalised” into polyhedral fault–bounded domains, whose dimension depend on the geometry of the fault zone network. Dashed arrows describe a closed path for fluid flow within each fault–bounded domain.

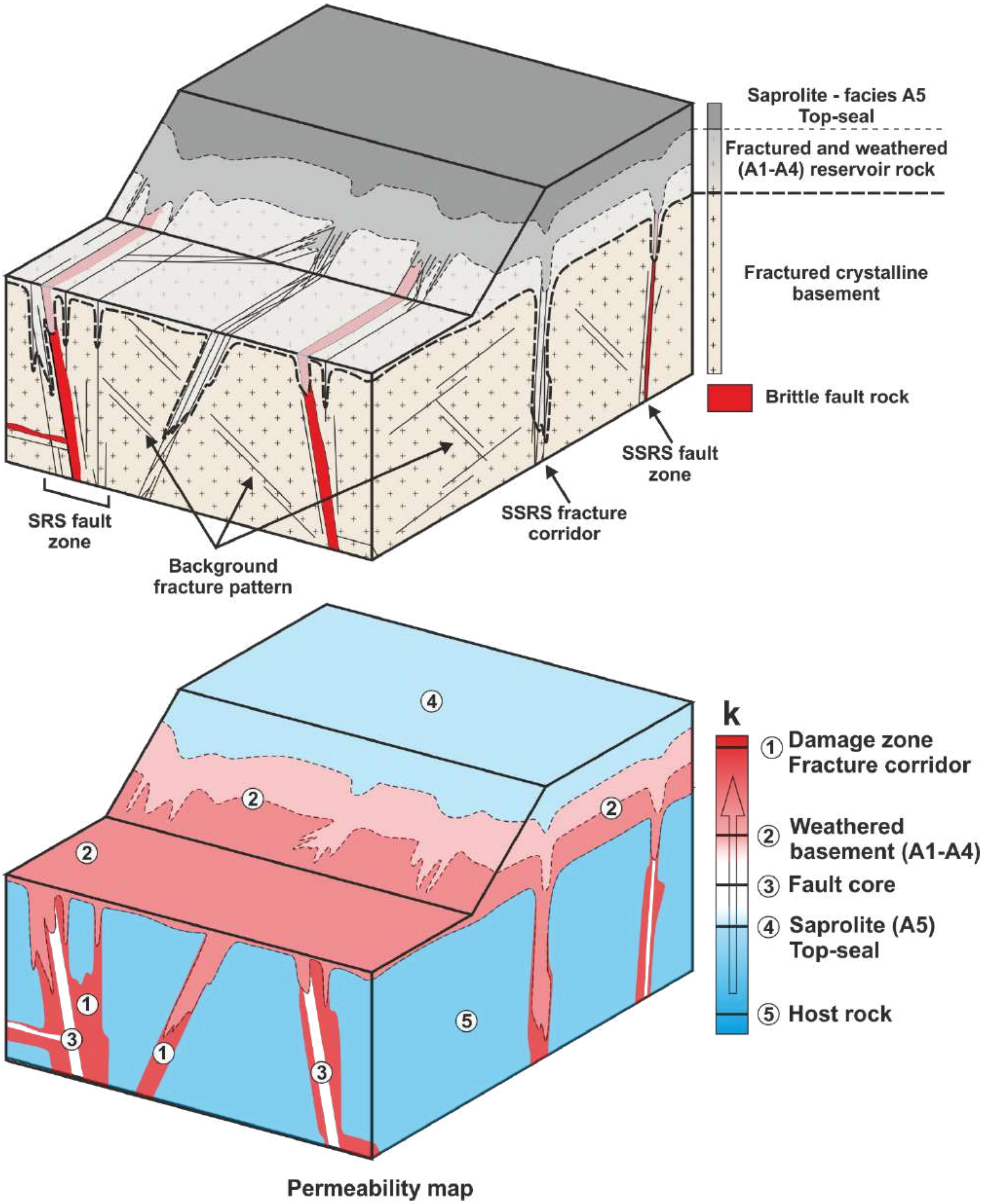

Figure 12. Block diagram summarising a conceptualised model of reservoir within fractured and weathered crystalline basement (not to scale). (a) The top–basement weathering profile overprints the fractured crystalline basement, exploiting the network of fractures and fault zones to penetrate to even great depth (down to to 300 m, Walter et al., 2018). (b) Schematic permeability map of the

conceptualised model described in (a). The reservoir is deformed by highly permeable fractures and fault zones (1) and contains the deepest portion of the weathering profile (2). Fault cores (3) are inherently more permeable than the unaltered host rock, thus acting as a conduit for fluid flow parallel to fault strike. The potential reservoir rocks (1–2) and potential fluid conduits (1 and 3) are overlain by the low permeability saprolitic horizon (4), which may act as top–seal layer. Weathering processes greatly increase the fluid storage and transport potential of the reservoir close to the top–basement surface, which is otherwise limited to the network of fractures and fault zones.

6. Conclusion

The matrix mechanical properties and permeability constrained by this study within the crystalline basement rocks exposed on Bømlo result from the prolonged and complex interplay between tectonics and lithosphere–atmosphere interactions (Fredin et al., 2017b). Brittle fracturing and weathering led to the development of secondary porosity at different scales: (a) meso–scale fracture porosity; (b) micro–porosity related to cataclastic processes and micro–fracturing; (c) micro–porosity related to mineral alteration and reaction–induced micro–fracturing. Thus, fault rock formation and weathering processes related to subaerial exposure and fluid percolation through deformation zones deeply affected both the mechanical strength and the matrix permeability of the RGD.

The fractured and weathered crystalline basement reservoir rocks are, therefore, composed of two main constituent elements: (1) the fractured crystalline basement and (2) the weathered/altered rock volume. The multiscale fracture network is composed of different types of fracture zones (SSRS fracture corridor, SSRS and SRS fault zones). Fault zones, either SSRS or SRS, represent zones of enhanced permeability with respect to the host crystalline basement and conduits for fluid flow parallel to the fault planes at all stages of evolution and at all scales (Caine et al. 1996). Meso–scale fractures spatially related to low strain and limited throw fracture corridors drastically enhance the overall permeability of the basement. Similarly, the formation of fault rocks, which are on average two orders of magnitude more permeable than the host rock, significantly increases the crystalline basement matrix permeability. They are characterised by anisotropic mechanical and permeability properties. In addition, they may act as partial seal/buffer layers to fluid flow within the high permeability structural network defined by fracture corridors and damage zones (Bruhn et al., 1994; Caine et al., 1996).

The comparison of weathering characteristics between different outcrops has allowed us to quantify the mechanical strength and permeability as a function of the actual position within the reconstructed weathering profile (Dewandel et al., 2006; Lothe et al., 2018). The weathering profile shows a progressive degradation of mechanical strength coupled to an initial increase in permeability during the incipient stages of weathering (up to 10 D, corresponding to its deepest portion), followed toward shallower depth by a significant decrease in permeability toward the more evolved weathering stages (down to 10^{-3} D). The matrix secondary permeability created during weathering greatly increases fluid storage and migration in a potential reservoir, which would otherwise be limited to volumes with sufficient structural permeability. Mature saprolitic horizons, on the other hand, may act as top–seal layer to the underlying permeable weathered products. As a consequence, weathering profiles may act both as reservoir and top–seal unit in sub–unconformity unconventional reservoirs (Braathen et al., 2018; Holdsworth et al., 2020; McCaffrey et al., 2020).

Fractured and weathered crystalline basement reservoirs are characterized by a significant mechanical heterogeneity, as inferred by the strikingly different mechanical properties of deformation zones, brittle fault rocks and weathering products. The mechanical heterogeneity is particularly developed toward the top–basement unconformity, where brittle deformation zones may be decorated by alteration products and abut the overlying weathering profile. The detailed quantification of the mechanical heterogeneity and its spatial distribution is therefore fundamental to optimize the planning strategies for the exploration and the operative exploitation of sub–unconformity unconventional reservoirs.

Acknowledgments

We thank Prof. Robert Holdsworth and an anonymous reviewer for the constructive comments and thorough reviews to the first version of the manuscript. Our research work was funded by the still ongoing BASE 2 project ("Basement fracturing and weathering onshore and offshore Norway—Genesis, age, and landscape development" – Part 2), a research initiative launched and steered by the Geological Survey of Norway and supported by Equinor ASA, Aker BP ASA, Lundin Energy Norway AS, Spirit Energy Norway AS, Wintershall Dea Norge, and NGU. We thank all BASE colleagues for continuous discussion and constructive inputs. We thank Erik James Ryan (NTNU) for the UAV surveys of the Goddo Fault Zone outcrop (Fig. 4).

989

References

Armitage, P.J., Faulkner, D.R., Worden, R.H., 2013. Caprock corrosion. Nature Geoscience 6, 79–80. https://doi.org/10.1038/ngeo1716

Aydin, A., 2009. ISRM Suggested method for determination of the Schmidt hammer rebound hardness: Revised version. International Journal of Rock Mechanics and Mining Sciences 46, 627–634. https://doi.org/10.1016/j.ijrmms.2008.01.020

Aydin, A., Basu, A., 2005. The Schmidt hammer in rock material characterization. Engineering Geology 81, 1–14. https://doi.org/10.1016/j.enggeo.2005.06.006

Banks, G., Bernstein, S., Salehi, S., Guarnieri, P., Bird, D., Hamblett, C., Peacock, D., Foster, J., 2019. Liverpool land basement high, Greenland: Visualising inputs for fractured crystalline basement reservoir models. Geological Survey of Denmark and Greenland Bulletin 43. https://doi.org/10.34194/GEUSB-201943-02-04

Belaidi, A., Bonter, D.A., Slightam, C., Trice, R.C., 2018. The Lancaster Field: Progress in opening the UK's fractured basement play. Petroleum Geology Conference Proceedings 8, 385–398. https://doi.org/10.1144/PGC8.20

Bell, R.E., Jackson, C.A.L., Whipp, P.S., Clements, B., 2014. Strain migration during multiphase extension: Observations from the northern North Sea. Tectonics 33, 1936–1963. https://doi.org/10.1002/2014TC003551

Bonter, D.A., Trice, R., 2019. An integrated approach for fractured basement characterization: The lancaster field, a case study in the UK. Petroleum Geoscience 25, 400–414. https://doi.org/10.1144/petgeo2018-152

Braathen, A., Abdel Fattah, M.M., Olaussen, S., Abdel-Gawad, G., Ogata, K., 2018. Basement-cover reservoir analogue in rift-margin fault blocks; Gulf of Suez Rift, Sinai, Egypt. Petroleum

Geoscience. https://doi.org/10.1144/petgeo2016-163

Brace, W.F., 1984. Permeability of Crystalline Rocks: New in Situ Measurements. Journal of Geophysical Research 89, 4327–4330. https://doi.org/10.1029/jb089ib06p04327

Bruhn, R.L., Parry, W.T., Yonkee, W.A., Thompson, T., 1994. Fracturing and hydrothermal alteration in normal fault zones. Pure and Applied Geophysics PAGEOPH 142, 609–644. https://doi.org/10.1007/BF00876057

Caine, J.S., Evans, J.P., Forster, C.B., 1996. Fault zone architecture and permeability structure. Geology 24, 1025–1028. https://doi.org/10.1130/0091-7613(1996)024<1025:FZAAPS>2.3.CO;2

Cappa, F., Rutqvist, J., 2011. Modeling of coupled deformation and permeability evolution during fault reactivation induced by deep underground injection of CO2. International Journal of Greenhouse Gas Control 5, 336–346. https://doi.org/10.1016/j.ijggc.2010.08.005

Coggan, J.S., Stead, D., Howe, J.H., Faulks, C.I., 2013. Mineralogical controls on the engineering behavior of hydrothermally altered granites under uniaxial compression. Engineering Geology 160, 89–102. https://doi.org/10.1016/j.enggeo.2013.04.001

Damsleth, E., Sangolt, V., Aamodt, G., 1998. Sub-seismic Faults Can Seriously Affect Fluid Flow in the Njord Field off Western Norway - A Stochastic Fault Modeling Case Study., SPE Annual Technical Conference and Exhibition. https://doi.org/10.2118/49024-MS

Demirdag, S., Yavuz, H., Altindag, R., 2009. The effect of sample size on Schmidt rebound hardness value of rocks. International Journal of Rock Mechanics and Mining Sciences 46, 725–730. https://doi.org/10.1016/j.ijrmms.2008.09.004

Dewandel, B., Lachassagne, P., Wyns, R., Maréchal, J.C., Krishnamurthy, N.S., 2006. A generalized 3-D geological and hydrogeological conceptual model of granite aquifers controlled by single or multiphase weathering. Journal of Hydrology 330, 260–284. https://doi.org/10.1016/j.jhydrol.2006.03.026

Douma, L.A.N.R., Regelink, J.A., Bertotti, G., Boersma, Q.D., Barnhoorn, A., 2019. The mechanical contrast between layers controls fracture containment in layered rocks. Journal of Structural Geology 127, 103856. https://doi.org/10.1016/j.jsg.2019.06.015

Evans, J.P., Forster, C.B., Goddard, J. V., 1997. Permeability of fault-related rocks, and implications for hydraulic structure of fault zones. Journal of Structural Geology 19, 1393–1404. https://doi.org/10.1016/S0191-8141(97)00057-6

Faulkner, D.R., 2004. A model for the variation in permeability of clay-bearing fault gouge with depth in the brittle crust. Geophysical Research Letters 31. https://doi.org/10.1029/2004GL020736

Faulkner, D.R., Jackson, C.A.L., Lunn, R.J., Schlische, R.W., Shipton, Z.K., Wibberley, C.A.J., Withjack, M.O., 2010. A review of recent developments concerning the structure, mechanics and fluid flow properties of fault zones. Journal of Structural Geology 32, 1557–1575. https://doi.org/10.1016/j.jsg.2010.06.009

Faulkner, D.R., Mitchell, T.M., Healy, D., Heap, M.J., 2006. Slip on "weak" faults by the rotation of regional stress in the fracture damage zone. Nature 444, 922–925. https://doi.org/10.1038/nature05353

Faulkner, D.R., Rutter, E.H., 1998. The gas permeability of clay-bearing fault gouge at 20 degrees C. 147, 147–156.

Filomena, C.M., Hornung, J., Stollhofen, H., 2014. Assessing accuracy of gas-driven permeability measurements: A comparative study of diverse Hassler-cell and probe permeameter devices. Solid Earth 5, 1–11. https://doi.org/10.5194/se-5-1-2014

Forbes Inskip, N.D., Browning, J., Meredith, P.G., Gudmundsson, A., 2020. Conditions for fracture arrest in layered rock sequences. Results in Geophysical Sciences 1–4, 100001. https://doi.org/10.1016/j.ringps.2020.100001

Forster, C.B., Evans, J.P., 1991. Hydrogeology of thrust faults and crystalline thrust sheets: results of combined field and modeling studies. 18, 979–982.

Fossen, H., Hurich, C.A., 2005. The Hardangerfjord Shear Zone in SW Norway and the North Sea: A large-scale low-angle shear zone in the Caledonian crust. Journal of the Geological Society 162, 675–687. https://doi.org/10.1144/0016-764904-136

Fossen, H., Schultz, R.A., Torabi, A., 2011. Conditions and implications for compaction band formation in the Navajo Sandstone, Utah. Journal of Structural Geology 33, 1477–1490. https://doi.org/10.1016/j.jsg.2011.08.001

Fredin, O., Viola, G., Zwingmann, H., Sorlie, R., Bronner, M., Lie, J.E., Grandal, E.M., Muller, A., Margreth, A., Vogt, C., Knies, J., 2017a. Correspondence: Reply to Challenges with dating weathering products to unravel ancient landscapes. Nature Communications 8, 1–2. https://doi.org/10.1038/s41467-017-01468-6

Fredin, O., Viola, G., Zwingmann, H., Sørlie, R., Brönner, M., Lie, J.E., Grandal, E.M., Müller, A., Margreth, A., Vogt, C., Knies, J., 2017b. The inheritance of a mesozoic landscape in western Scandinavia. Nature Communications 8. https://doi.org/10.1038/ncomms14879

Gabrielsen, R.H., Braathen, A., 2014. Models of fracture lineaments - Joint swarms, fracture corridors and faults in crystalline rocks, and their genetic relations. Tectonophysics 628, 26–44. https://doi.org/10.1016/j.tecto.2014.04.022

Gabrielsen, R.H., Kyrkjebø, R., Faleide, J.I., Fjeldskaar, W., Kjennerud, T., 2001. The Cretaceous post-rift basin configuration of the northern North Sea. Petroleum Geoscience. https://doi.org/10.1144/petgeo.7.2.137

Gee, D.G., Fossen, H., Henriksen, N., Higgins, A.K., 2008. From the early Paleozoic platforms of Baltica and Laurentia to the Caledonide Orogen of Scandinavia and Greenland. Episodes 31, 44–51. https://doi.org/10.18814/epiiugs/2008/v31i1/007

Géraud, Y., Rosener, M., Surma, F., Place, J., Le Garzic, É., Diraison, M., 2010. Physical properties of fault zones within a granite body: Example of the Soultz-sous-Forêts geothermal site. Comptes Rendus - Geoscience 342, 566–574. https://doi.org/10.1016/j.crte.2010.02.002

Gomila, R., Arancibia, G., Mitchell, T.M., Cembrano, J.M., Faulkner, D.R., 2016. Palaeopermeability structure within fault-damage zones: A snap-shot from microfracture analyses in a strike-slip system. Journal of Structural Geology 83, 103–120. https://doi.org/10.1016/j.jsg.2015.12.002

Goodfellow, B.W., Hilley, G.E., Webb, S.M., Sklar, L.S., Moon, S., Olson, C.A., 2016. The chemical, mechanical, and hydrological evolution of weathering granitoid. Journal of Geohpysical Research: Earth Surface 1–26. https://doi.org/10.1002/2016JF003822.Received

Gudmundsson, A., Simmenes, T.H., Larsen, B., Philipp, S.L., 2010. Effects of internal structure and local stresses on fracture propagation, deflection, and arrest in fault zones. Journal of Structural Geology 32, 1643–1655. https://doi.org/10.1016/j.jsg.2009.08.013

Hayes, J.L., Riebe, C.S., Steven Holbrook, W., Flinchum, B.A., Hartsough, P.C., 2019. Porosity production in weathered rock: Where volumetric strain dominates over chemical mass loss. Science Advances 5, 1–12. https://doi.org/10.1126/sciadv.aao0834

Healy, D., 2008. Damage patterns, stress rotations and pore fluid pressures in strike-slip fault zones. Journal of Geophysical Research: Solid Earth 113, 1–16. https://doi.org/10.1029/2008JB005655

Healy, D., Rizzo, R.E., Cornwell, D.G., Farrell, N.J.C., Watkins, H., Timms, N.E., Gomez-Rivas, E., Smith, M., 2017. FracPaQ: A MATLAB$^{\mathrm{TM}}$ toolbox for the quantification of fracture patterns. Journal of Structural Geology 95, 1–16. https://doi.org/10.1016/j.jsg.2016.12.003

Høien, A.H., Nilsen, B., Olsson, R., 2019. Main aspects of deformation and rock support in Norwegian road tunnels. Tunnelling and Underground Space Technology 86, 262–278. https://doi.org/10.1016/j.tust.2019.01.026

Holdsworth, R.E., McCaffrey, K.J.W., Dempsey, E., Roberts, N.M.W., Hardman, K., Morton, A., Feely, M., Hunt, J., Conway, A., Robertson, A., 2019. Natural fracture propping and earthquake-induced oil migration in fractured basement reservoirs. Geology 47, 700–704. https://doi.org/10.1130/G46280.1

Holdsworth, R.E., Trice, R., Hardman, K., McCaffrey, K.J.W., Morton, A., Frei, D., Dempsey, E., Bird, A., Rogers, S., 2020. The nature and age of basement host rocks and fissure fills in the Lancaster field fractured reservoir, West of Shetland. Journal of the Geological Society jgs2019-142. https://doi.org/10.1144/jgs2019-142

Howell, J.A., Martinius, A.W., Good, T.R., 2014. The application of outcrop analogues in geological modelling: a review, present status and future outlook. Geological Society, London, Special Publications 387, 1–25. https://doi.org/10.1144/sp387.12

Jeanne, P., Guglielmi, Y., Cappa, F., 2013. Hydromechanical heterogeneities of a mature fault zone: Impacts on fluid flow. Groundwater 51, 880–892. https://doi.org/10.1111/gwat.12017

Jeanne, P., Guglielmi, Y., Rutqvist, J., Nussbaum, C., Birkholzer, J., 2017. Field characterization of elastic properties across a fault zone reactivated by fluid injection. Journal of Geophysical Research: Solid Earth 122, 6583–6598. https://doi.org/10.1002/2017JB014384

Jones, R.R., McCaffrey, K.J.W., Imber, J., Wightman, R., Smith, S.A.F., Holdsworth, R.E., Clegg, P., De Paola, N., Healy, D., Wilson, R.W., 2008. Calibration and validation of reservoir models: The importance of high resolution, quantitative outcrop analogues. Geological Society Special Publication 309, 87–98. https://doi.org/10.1144/SP309.7

Kitchka, A.A., Petrovskyy, O.P., Fedchenko, T.O., Kuzmanenko, G.O., Solomyanyi, A.R., 2017.

Analogue Outcrops Study of the Weathered Crystalline Crust Benefits for Basement Reservoirs Exploration in Ukraine. European Association of Geoscientists & Engineers, 1–5. https://doi.org/10.3997/2214-4609.201700881

Koning, T., 2003. Oil and gas production from basement reservoirs: Examples from Indonesia, USA and Venezuela. Geological Society Special Publication. https://doi.org/10.1144/GSL.SP.2003.214.01.05

Leclère, H., Cappa, F., Faulkner, D.R., Fabbri, O., Armitage, P., Blake, O., 2015. Development and maintenance of fluid overpressures in crustal fault zones by elastic compaction and implications for earthquake swarms. Journal of Geophysical Research: Solid Earth 120, 4450–4473. https://doi.org/10.1002/2014JB011759

Long, J.C.S., Remer, J.S., Wilson, C.R., Witherspoon, P.A., 1982. Porous media equivalents for networks of discontinuous fractures. Water Resources Research 18, 645–658. https://doi.org/10.1029/WR018i003p00645

Lothe, A.E., Emmel, B., Bergmo, P.E., Akervoll, I., Todorovic, J., Bhuiyan, M.H., Knies, J., 2018. Porosity, permeability and compaction trends for Scandinavian regoliths. Marine and Petroleum Geology 92, 319–331. https://doi.org/10.1016/j.marpetgeo.2017.10.027

Lundmark, A.M., Sæther, T., Sørlie, R., 2014. Ordovician to silurian magmatism on the Utsira High, North Sea: Implications for correlations between the onshore and offshore Caledonides. Geological Society Special Publication 390, 513–523. https://doi.org/10.1144/SP390.21

Luthi, S.M., 2005. Fractured reservoir analysis using modern geophysical well techniques: Application to basement reservoirs in Vietnam. Geological Society Special Publication 240, 95–106. https://doi.org/10.1144/GSL.SP.2005.240.01.08

McCaffrey, K.J.W., Holdsworth, R.E., Pless, J., Franklin, B.S.G., Hardman, K., 2020. Basement reservoir plumbing: fracture aperture, length and topology analysis of the Lewisian Complex, NW Scotland. Journal of the Geological Society. https://doi.org/https://doi.org/10.1144/jgs2019-143 This

Migoń, P., Thomas, M.F., 2002. Grus weathering mantles - Problems of interpretation. Catena 49, 5–24. https://doi.org/10.1016/S0341-8162(02)00014-0

Mitchell, T.M., Faulkner, D.R., 2012. Towards quantifying the matrix permeability of fault damage zones in low porosity rocks. Earth and Planetary Science Letters 339–340, 24–31. https://doi.org/10.1016/j.epsl.2012.05.014

Niemeijer, A.R., Spiers, C.J., 2005. Influence of phyllosilicates on fault strength in the brittle-ductile transition: Insights from rock analogue experiments. Geological Society Special Publication 245, 303–327. https://doi.org/10.1144/GSL.SP.2005.245.01.15

Ortega, O.J., Marrett, R.A., Laubach, S.E., 2006. A scale-independent approach to fracture intensity and average spacing measurement. American Association of Petroleum Geologists Bulletin 90, 193–208. https://doi.org/10.1306/08250505059

Place, J., Géraud, Y., Diraison, M., Herquel, G., Edel, J.B., Bano, M., Le Garzic, E., Walter, B., 2016. Structural control of weathering processes within exhumed granitoids: Compartmentalisation of geophysical properties by faults and fractures. Journal of Structural Geology 84, 102–119. https://doi.org/10.1016/j.jsg.2015.11.011

Primaleon, L.P., McCaffrey, K.J.W., Holdsworth, R.E., 2020. Fracture attribute and topology characteristics of a geothermal reservoir: Southern Negros, Philippines. Journal of the Geological Society 177, 1092 LP – 1106. https://doi.org/10.1144/jgs2019-126

Rempe, M., Mitchell, T.M., Renner, J., Smith, S.A.F., Bistacchi, A., Di Toro, G., 2018. The Relationship Between Microfracture Damage and the Physical Properties of Fault-Related Rocks: The Gole Larghe Fault Zone, Italian Southern Alps. Journal of Geophysical Research: Solid Earth 123, 7661–7687. https://doi.org/10.1029/2018JB015900

Riber, L., Driese, S.G., Stinchcomb, G.E., Dypvik, H., Sørlie, R., 2019a. Reconstructing a high paleolatitude Mesozoic paleoenvironment from a truncated and deeply buried regolith, Norwegian North Sea. Palaeogeography, Palaeoclimatology, Palaeoecology 528, 60–77. https://doi.org/10.1016/J.PALAEO.2019.04.031

Riber, L., Driese, S.G., Stinchcomb, G.E., Dypvik, H., Sørlie, R., 2019b. Reconstructing a high paleolatitude Mesozoic paleoenvironment from a truncated and deeply buried regolith, Norwegian North Sea. Palaeogeography, Palaeoclimatology, Palaeoecology 528, 60–77. https://doi.org/10.1016/j.palaeo.2019.04.031

Riber, L., Dypvik, H., Sørlie, R., 2015. Altered basement rocks on the Utsira High and its surroundings, Norwegian North Sea. Norwegian Journal of Geology 95, 57–89. https://doi.org/10.17850/njg95-1-04

Riber, L., Dypvik, H., Sørlie, R., Ferrell, R.E., 2016. Clay minerals in deeply buried paleoregolith profiles, Norwegian North Sea. Clays and Clay Minerals 64, 588–607. https://doi.org/10.1346/CCMN.2016.064036

Riber, L., Dypvik, H., Sørlie, R., Naqvi, S.A.A.E.M., Stangvik, K., Oberhardt, N., Schroeder, P.A., 2017. Comparison of deeply buried paleoregolith profiles, Norwegian North Sea, with outcrops from southern Sweden and Georgia, USA — Implications for petroleum exploration. Palaeogeography, Palaeoclimatology, Palaeoecology 471, 82–95. https://doi.org/10.1016/j.palaeo.2017.01.043

Roberts, D., 2003. The Scandinavian Caledonides: Event chronology, palaeogeographic settings and likely modern analogues. Tectonophysics 365, 283–299. https://doi.org/10.1016/S0040-1951(03)00026-X

Rutqvist, J., Stephansson, O., 2003. The role of hydrochemical coupling in fractured rock engineering. Hydrogeology Journal 11, 7–40. https://doi.org/10.1007/s10040-002-0241-5

Ryan, R.J., O’Beirne-Ryan, A.M., Zentilli, M., 2005. Rounded cobbles that have not travelled far: Incorporation of corestones from saprolites in the South Mountain area of southern Nova Scotia, Canada. Sedimentology 52, 1109–1121. https://doi.org/10.1111/j.1365-3091.2005.00730.x

Scheiber, T., Viola, G., 2018. Complex Bedrock Fracture Patterns: A Multipronged Approach to Resolve Their Evolution in Space and Time. Tectonics 37, 1030–1062. https://doi.org/10.1002/2017TC004763

Scheiber, T., Viola, G., Wilkinson, C.M., Ganerød, M., Skår, Ø., Gasser, D., 2016. Direct40Ar/39Ar dating of Late Ordovician and Silurian brittle faulting in the southwestern Norwegian Caledonides. Terra Nova 28, 374–382. https://doi.org/10.1111/ter.12230

Scibek, J., 2020. Multidisciplinary database of permeability of fault zones and surrounding protolith rocks at world-wide sites. Scientific Data 7, 1–14. https://doi.org/10.1038/s41597-020-0435-5

Sclater, J.G., Christie, P.A.F., 1980. Continental stretching: An explanation of the Post-Mid-Cretaceous subsidence of the central North Sea Basin. Journal of Geophysical Research: Solid Earth. https://doi.org/10.1029/jb085ib07p03711

Shea, W.T., Kronenberg, A.K., 1993. Strength and anisotropy of foliated rocks with varied mica contents. Journal of Structural Geology 15, 1097–1121. https://doi.org/10.1016/0191-8141(93)90158-7

Sibson, R.H., Rowland, J. V., 2003. Stress, fluid pressure and structural permeability in seismogenic crust, North Island, New Zealand. Geophysical Journal International 154, 584–594. https://doi.org/10.1046/j.1365-246X.2003.01965.x

Slagstad, T., Davidsen, B., Stephen Daly, J., 2011. Age and composition of crystalline basement rocks on the norwegian continental margin: Offshore extension and continuity of the Caledonian-Appalachian orogenic belt. Journal of the Geological Society 168, 1167–1185. https://doi.org/10.1144/0016-76492010-136

Smart, K.J., Ofoegbu, G.I., Morris, A.P., McGinnis, R.N., Ferrill, D.A., 2014. Geomechanical modeling of hydraulic fracturing: Why mechanical stratigraphy, stress state, and pre-existing structure matter. AAPG Bulletin 98, 2237–2261. https://doi.org/10.1306/07071413118

Souque, C., Knipe, R.J., Davies, R.K., Jones, P., Welch, M.J., Lorenz, J., 2019. Fracture corridors and fault reactivation: Example from the Chalk, Isle of Thanet, Kent, England. Journal of Structural Geology 122, 11–26. https://doi.org/10.1016/j.jsg.2018.12.004

Staněk, M., Géraud, Y., 2019. Granite microporosity changes due to fracturing and alteration: Secondary mineral phases as proxies for porosity and permeability estimation. Solid Earth 10, 251–274. https://doi.org/10.5194/se-10-251-2019

Steefel, C.I., Mäher, K., 2009. Fluid-rock interaction: A reactive transport approach. Reviews in Mineralogy and Geochemistry 70, 485–532. https://doi.org/10.2138/rmg.2009.70.11

Steer, P., Bigot, A., Cattin, R., Soliva, R., 2011. In-situ characterization of the effective elasticity of a fault zone, and its relationship to fracture spacing. Journal of Structural Geology 33, 1541–1553. https://doi.org/10.1016/j.jsg.2011.09.009

Stober, I., Bucher, K., 2015. Hydraulic conductivity of fractured upper crust: Insights from hydraulic tests in boreholes and fluid-rock interaction in crystalline basement rocks. Geofluids 15, 161–178. https://doi.org/10.1111/gfl.12104

Stober, I., Bucher, K., 2007. Hydraulic properties of the crystalline basement. Hydrogeology Journal 15, 213–224. https://doi.org/10.1007/s10040-006-0094-4

Tanner, D.C., Buness, H., Igel, J., Günther, T., Gabriel, G., Skiba, P., Plenefisch, T., Gestermann, N., Walter, T.R., 2019. Fault detection, Understanding Faults: Detecting, Dating, and Modeling. https://doi.org/10.1016/B978-0-12-815985-9.00003-5

Tartaglia, G., Viola, G., van der Lelij, R., Scheiber, T., Ceccato, A., Schönenberger, J., 2020. "Brittle structural facies” analysis: A diagnostic method to unravel and date multiple slip events of long-lived faults. Earth and Planetary Science Letters 545, 116420. https://doi.org/10.1016/j.epsl.2020.116420

Torabi, A., Alaei, B., Ellingsen, T.S.S., 2018. Faults and fractures in basement rocks, their architecture, petrophysical and mechanical properties. Journal of Structural Geology 117, 256–263. https://doi.org/10.1016/j.jsg.2018.07.001

Torabi, A., Berg, S.S., 2011. Scaling of fault attributes: A review. Marine and Petroleum Geology 28, 1444–1460. https://doi.org/10.1016/j.marpetgeo.2011.04.003

Trice, R., Hiorth, C., Holdsworth, R., 2019. Fractured basement play development on the UK and Norwegian rifted margins. Geological Society, London, Special Publications SP495-2018–174. https://doi.org/10.1144/sp495-2018-174

van Noort, R., Yarushina, V., 2019. Water, CO 2 and Argon Permeabilities of Intact and Fractured Shale Cores Under Stress. Rock Mechanics and Rock Engineering 52, 299–319. https://doi.org/10.1007/s00603-018-1609-8

Vignaroli, G., Giallini, S., Polpetta, F., Sirianni, P., Gaudiosi, I., Simionato, M., Razzano, R., Pagliaroli, A., Moscatelli, M., Mancini, M., Cavinato, G.P., Avalle, A., 2019. Domains of seismic noise response in faulted limestone (central Apennines, Italy): insights into fault-related site effects and seismic hazard. Bulletin of Engineering Geology and the Environment 78, 2749–2768. https://doi.org/10.1007/s10064-018-1276-8

Viola, G., Scheiber, T., Fredin, O., Zwingmann, H., Margreth, A., Knies, J., 2016. Deconvoluting complex structural histories archived in brittle fault zones. Nature Communications 7, 1–10. https://doi.org/10.1038/ncomms13448

Walsh, J.J., Watterson, J., Bailey, W.R., Childs, C., 1999. Fault relays, bends and branch-lines. Journal of Structural Geology. https://doi.org/10.1016/S0191-8141(99)00026-7

Walsh, J.J., Watterson, J., Heath, A., Gillespie, P.A., Childs, C., 1998. Assessment of the effects of sub-seismic faults on bulk permeabilities of reservoir sequences. Geological Society Special Publication 127, 99–114. https://doi.org/10.1144/GSL.SP.1998.127.01.08

Walter, B., Géraud, Y., Bartier, D., Kluska, J.M., Diraison, M., Morlot, C., Raisson, F., 2018. Petrophysical and mineralogical evolution of weathered crystalline basement in western Uganda: Implications for fluid transfer and storage. AAPG Bulletin 102, 1035–1065. https://doi.org/10.1306/0810171610917171

Watkins, H., Bond, C.E., Healy, D., Butler, R.W.H., 2015. Appraisal of fracture sampling methods and a new workflow tocharacterise heterogeneous fracture networks at outcrop. Journal of Structural Geology 72, 67–82. https://doi.org/10.1016/j.jsg.2015.02.001

Watkins, H., Healy, D., Bond, C.E., Butler, R.W.H., 2018. Implications of heterogeneous fracture distribution on reservoir quality; an analogue from the Torridon Group sandstone, Moine Thrust Belt, NW Scotland. Journal of Structural Geology 108, 180–197. https://doi.org/10.1016/j.jsg.2017.06.002

Wibberley, C.A.J., Yielding, G., Di Toro, G., 2008. Recent advances in the understanding of fault zone internal structure: A review. Geological Society Special Publication 299, 5–33. https://doi.org/10.1144/SP299.2

Wilson, J.E., Chester, J.S., Chester, F.M., 2003. Microfracture analysis of fault growth and wear processes, Punchbowl Fault, San Andreas system, California. Journal of Structural Geology 25, 1855–1873. https://doi.org/10.1016/S0191-8141(03)00036-1

Zauyah, S., Schaefer, C.E.G.R., Simas, F.N.B., 2018. Chapter 3 Saprolites, Interpretation of Micromorphological Features of Soils and Regoliths. Elsevier B.V. https://doi.org/10.1016/B978-0-444-63522-8.00003-6

Zhang, S., Tullis, T.E., 1998. The effect of fault slip on permeability and permeability anisotropy in quartz gouge. Tectonophysics 295, 41–52. https://doi.org/10.1016/S0040-1951(98)00114-0